

Cite this: *RSC Adv.*, 2017, 7, 8606

Cadmium and lead remediation using magnetic and non-magnetic sustainable biosorbents derived from *Bauhinia purpurea* pods†

Rupa Sharma,^a Ankur Sarswat,^a Charles U. Pittman Jr.^b and Dinesh Mohan^{*a}

Bauhinia purpurea (Kaniar) pods were dried, powdered, and utilized for cadmium and lead removal. *Bauhinia purpurea* (Kaniar) pod powders (KPP) were converted into magnetic *Bauhinia purpurea* (Kaniar) powders (MKPP) by co-precipitation. Iron(II) sulfate and iron(III) sulfate were used as iron precursors. The biosorbents were extensively characterized using zero point charge measurements (pH_{PZC}), ultimate and proximate analyses, Fourier transform infrared (FTIR) and FT-Raman spectroscopy, transmission electron microscopy (TEM), X-ray diffraction (XRD), BET surface area (S_{BET}) measurements, physical properties measurement system (PPMS), scanning electron microscopy (SEM) and energy dispersive X-ray fluorescence (EDXRF) techniques. The S_{BET} of MKPP ($52.0 \text{ m}^2 \text{ g}^{-1}$) was higher than KPP ($1.8 \text{ m}^2 \text{ g}^{-1}$). Optimum Cd^{2+} and Pb^{2+} removal by KPP and MKPP was obtained at pH 5.0 and 4.5, respectively. Metal–ligand chelation, ion-exchange and hydrogen bonding were possible mechanisms for Cd^{2+} and Pb^{2+} removal. KPP and MKPP showed maximum Langmuir adsorption capacities of 11.1 and 4.8 mg g^{-1} for Cd^{2+} and 16.4 and 14.1 for Pb^{2+} , respectively. Lead and cadmium kinetic data were best described using a pseudo-second-order equation. Cd^{2+} and Pb^{2+} removal was affected by the presence of Cu^{2+} during adsorption from a multicomponent aqueous environment. Cd^{2+} and Pb^{2+} remediation from actual groundwater was demonstrated. Fixed-bed studies for Pb^{2+} removal by KPP were also performed with a column capacity of 18.8 mg g^{-1} (column dia 2.0 cm; column length 40 cm; bed height 6.0 cm; pH 4.5; flow rate 5.0 mL min^{-1} ; Pb^{2+} conc. 10 mg L^{-1}). Spent KPP was regenerated using 0.1 N HCl. Approximately 85% of total Pb^{2+} recovery was achieved using 100 mL 0.1 N HCl.

Received 15th October 2016
Accepted 23rd November 2016

DOI: 10.1039/c6ra25295h

www.rsc.org/advances

1. Introduction

Clean water is a most valuable natural resource.¹ Water pollution due to heavy metals, dyes, pesticides, pharmaceuticals, arsenic, and fluoride contamination is increasing.² Heavy metals, in particular, are emerging as one of the most common class of water pollutants.³ Heavy metals are capable of inducing toxic effects in organisms when present above their permissible concentrations.⁴ Cadmium and lead are highly toxic priority pollutants.⁵ Cadmium contamination in groundwater originates with the manufacturing of alloys, batteries, pigments, plastics, mining and refining processes.^{6,7} Cadmium causes severe damage to kidneys and bones and is associated with itai-itai disease. Its accumulation in the human body leads to erythrocyte destruction, nausea, salivation, diarrhea, muscular cramps, renal degradation, chronic pulmonary problems, and

skeletal deformity.⁸ Cadmium ions are unlikely to hydrolyze at $\text{pH} < 8$ but tend to exist as hydroxo-complexes at $\text{pH} > 11$.⁹

Mining, smelting, fossil fuels combustion, solid waste incineration, batteries, paints, cables, ceramics and glass manufacturing are common anthropogenic sources of lead contamination in groundwater.^{10,11} Acute lead poisoning may result to headache, irritability, abdominal pain and various symptoms related to nervous systems. Children are particularly susceptible to lead poisoning due to the high gastro-intestinal barrier and permeable blood–brain barrier.¹² The World Health Organization¹³ and Bureau of Indian Standards^{14,15} permissible limits for cadmium and lead in drinking water are 0.003 and 0.01 mg L^{-1} , respectively. Common methods deployed for aqueous Cd^{2+} and Pb^{2+} removal include filtration, chemical precipitation, ion-exchange, membrane process, electrodeposition and adsorption.¹⁶

Adsorption is a simple, effective and economically viable approach,⁴ widely used to remediate heavy metals and other pollutants.¹⁷ Several adsorbents have been used for Pb^{2+} and Cd^{2+} remediation, including clays, minerals (goethite, hydroxyapatite and calcite), and calcareous soils.¹⁸ Industrial wastes used as Pb^{2+} and Cd^{2+} adsorbents include slags, sludges, modified asphaltite ashes, fly ash chitosan, zeolite, humic acid,

^aSchool of Environmental Sciences, Jawaharlal Nehru University, New Delhi 110067, India. E-mail: dm_1967@hotmail.com; Fax: +91-11-26704616; Tel: +91-11-26704616

^bDepartment of Chemistry, Mississippi State University, Mississippi State, MS 39762, USA

† Electronic supplementary information (ESI) available. See DOI: 10.1039/c6ra25295h



and sesquioxides (iron, aluminium, or manganese oxides).¹⁸ Some bio-materials, such as bark, dead biomass, modified wool, moss, peat and seaweed, were also applied for aqueous Cd^{2+} and Pb^{2+} removal.¹⁹ Nitrilotriacetic acid anhydride modified ligno-cellulosic material was also used for cadmium and lead removal.²⁰ Reviews of contaminant remediation of water by various biosorbents have appeared.^{21,22} Activated carbon, the most common adsorbent used to remediate many pollutants²³ has high production costs.²⁴ Therefore, heavy metal removal using a low cost adsorbent is essential to encourage remediation.

Biosorption uses the ability of biological materials to accumulate aqueous heavy metals by metabolically mediated or physico-chemical uptake pathways.²⁵ Biosorption can exhibit several advantages including higher sorption capacity, regeneration, and adsorbate recovery.²⁶ Olive stones and sugarcane bagasse,²⁷ marine microphytes,²⁸ *Spirulina*,²⁹ *Camellia sinensis*,³⁰ pectin based adsorbent³¹ and fungal and wood adsorbents³² were tested for aqueous lead and cadmium removal in single and binary systems. Recently, biosorbents used for heavy metals were reviewed.³³

Bauhinia purpurea, commonly known as Kaniar or Kachnar, is a small tree. The purple *Bauhinia* tree (*Bauhinia purpurea*) is native to lower Himalayan slopes extend up to Assam and throughout the Indian Peninsula. *Bauhinia purpurea* is also found in Myanmar, Sri Lanka and Southern China.³⁴ *Bauhinia purpurea* leaves, flowers, flower buds, and young pods are edible³⁵ and have medicinal value, exhibiting antioxidant,³⁶ anti-cancer,³⁷ anti-microbial,³⁸ and nephroprotective³⁹ activities. *Bauhinia purpurea* can withstand aqueous pollutants.⁴⁰

Also, biomass from *Bauhinia* leaves was used for dye removal from wastewater.⁴¹ Thus, we selected, dried, and powdered *Bauhinia* pods for use as a sustainable biosorbent. *Bauhinia purpurea* pod powder was also magnetized to prepare magnetic biosorbent. Magnetization allows easy recovery of exhausted biosorbent from aqueous systems using a simple magnet.

2. Material and methods

2.1. Reagents and equipment

All the chemicals used in the study were either AR or GR grade. Lead nitrate, $\text{Pb}(\text{NO}_3)_2$ ($\geq 99\%$), cadmium nitrate, $\text{Cd}(\text{NO}_3)_2$ ($\geq 99\%$), iron(II) sulfate, FeSO_4 (99.5%), and sodium hydroxide, NaOH (98%) were obtained from Merck, India. Iron(III) sulfate, $\text{Fe}_2(\text{SO}_4)_3$ (minimum assay 20.50%) was purchased from CDH, India.

Cd^{2+} and Pb^{2+} stock solutions were prepared in doubly distilled water. Solution pHs were adjusted using 0.1 M nitric acid and sodium hydroxide dilute solutions.

2.1.1. Magnetic and non-magnetic biosorbents development. Fresh *Bauhinia purpurea* pods were collected, washed, and then sun-dried. Dried pods were ground and sieved into different particle sizes. The 30–50 B.S.S. mesh size range was selected for the sorption experiments. Selected samples were washed several times with distilled water to remove any color. Finally, this powder was dried overnight at 70 °C and stored in airtight containers for further use (Fig. 1). This biosorbent was designated as KPP.

KPP was magnetized using a chemical precipitation method with modifications discussed earlier.⁵ Briefly, 20 g of KPP was

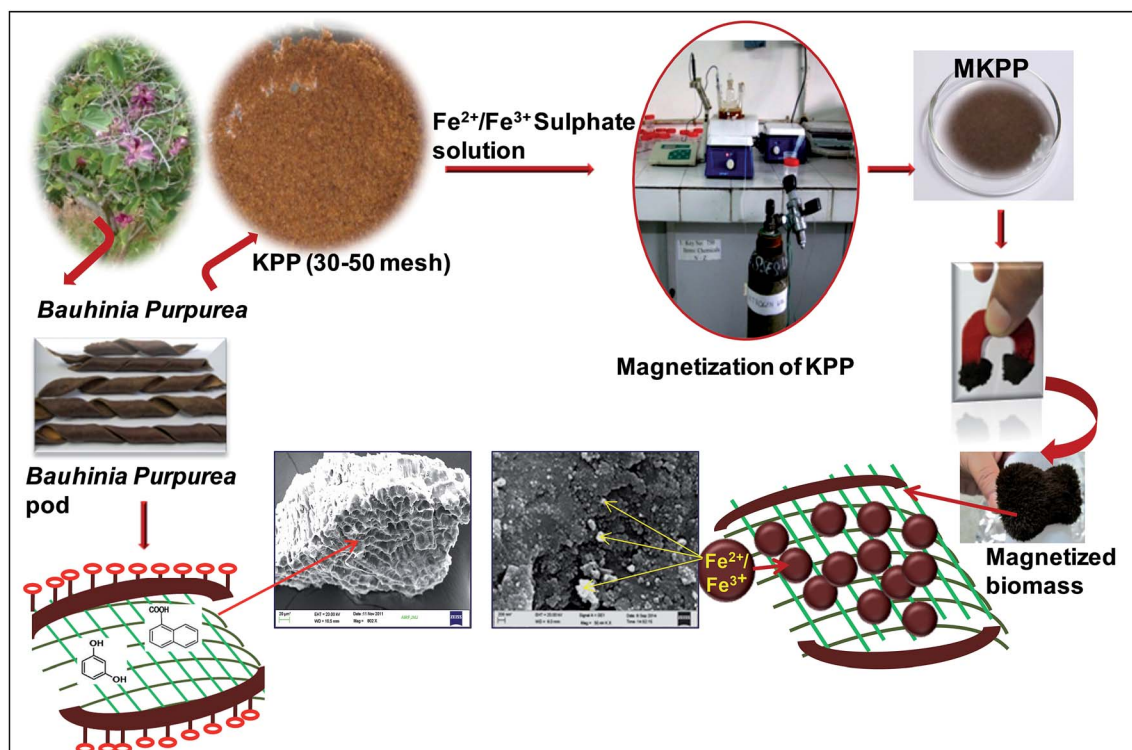


Fig. 1 Schematic diagram for KPP and MKPP development, recovery of spent KPP and MKPP.



stirred in 200 mL of double distilled water for 1 h. Ferrous sulfate (8 g in 60 mL DW) and ferric sulfate (7.4 g in 20 mL DW) solutions were mixed together. This ferrous–ferric solution was added to the KPP suspension in a three neck round bottom flask. The suspension was agitated for 1 h under nitrogen. Then the pH was raised to pH 10–11 using a freshly prepared 10 M NaOH. The iron oxide nanoparticles started precipitating on KPP surfaces and inner pores during the pH rise. The suspension was aged (24 h), filtered, and washed using distilled water until the pH was constant at ~ 7.0 . Finally, the magnetic biosorbent was washed using ethanol and dried overnight at 70 °C. The magnetic biosorbent was designated as MKPP. Fig. 1 shows the schematic diagram for MKPP development.

2.1.2. Characterization. pH_{ZPC} is the pH at which the net charge on the surface resulting from the adsorption on the surface is zero. Surfaces in aqueous solutions are positively charged below their pH_{ZPC} , thereby favor anion adsorption. Surfaces are negatively charged above their pH_{ZPC} and favor cation adsorption. The zero point charge (pH_{ZPC}) of KPP and MKPP were measured at 1, 2, 4, 6, 8 and 10 g L⁻¹. Samples were added in doubly distilled water. Suspensions were brought to a series of pH values (pH 2, 3, 4, 5, 6, 7, 8, 9, 10), agitated for 48 h at room temperature, and after 48 h, the equilibrium pH values were measured.

An automated surface area and porosity analyzer (model ASAP 2020, Micromeritics) was used for the surface area, total pore volume and pore size analyses of KPP and MKPP. Biomass samples (0.15 g) were out-gassed at 250 °C for 12 h at $<10^{-3}$ Torr, prior to nitrogen adsorption measurements.

Dried samples were degassed prior to the analysis. The Brunauer–Emmett–Teller (BET) surface area was calculated from the BET adsorption plot. The Barrett–Joyner–Halenda (BJH)⁴² adsorption–desorption isotherm was used to determine the pore size distribution. The total micropore volume (W_0) was estimated by the Dubinin–Radushkevich (D–R) method.^{43,44}

The biosorbents moisture, volatile and ash content were analyzed by ASTM method.⁴⁵ The C, H and N were determined using an elemental analyzer (model EURO EA 3000). Ash content was determined by incinerating a 1 g sample in a muffle furnace (Scientech, India) at 750 °C for 6 h.

Surface morphology and elemental composition of KPP and MKPP were examined using a scanning electron microscope (model EVO40, Zeiss) at an accelerating voltage of 10 000 V, working distance 9900 μm and emission current 13 300 nA equipped with Bruker EDX system. Samples were gold coated to make a conductive layer and mounted on a copper stub using a double stick carbon tape.⁵

KPP and MKPP elemental analyses were carried out on an energy dispersive X-ray fluorescence spectrometer (model Epsilon 5, PANalytical). KPP and MKPP were mixed with boric acid and pressed using an Insmart System (INSMART XRF 40) at an applied pressure of 5 t. The pellet size and exposure area were 34 mm and 8 mm, respectively.

The FTIR spectra of KPP and MKPP were recorded with a FTIR spectrometer (model 7000, Varian) on KBR pellets (1 : 20 ratio) formed at a pressure of 10 t.

KPP and MKPP X-ray diffraction (XRD) patterns were obtained on a powder XRD system (model X'Pert PRO, PANalytical) using

Cu-K α radiation ($\lambda = 1.54 \text{ \AA}$) at 45 kV and 40 mA. The samples were scanned from 10 to 90° with a scan speed of 2° min⁻¹.

KPP and MKPP morphologies were examined by TEM (model JEM 2100F, JEOL) at 200 kV. Samples were ultrasonicated in ethanol for 10 min, vacuum dried, and loaded on an amorphous carbon-coated copper grid.

The MKPP magnetic hysteresis loop was recorded with a Physical Property Measurement System (PPMS) (model T-415, Cryogenic, USA) at 5 K and 300 K. Powdered samples were filled in gelatinous capsule and sealed with Teflon tape.

The FT-Raman spectra of KPP and MKPP were recorded with FT-Raman spectrometer (model Varian FT-Raman) in the range of 4000–100 cm⁻¹.

2.2. Sorption procedure

Sorption equilibrium and dynamic studies were conducted. Sorption parameters are necessary to design a fixed-bed reactor. Biosorption studies for Pb²⁺ and Cd²⁺ removal were performed in batch and column modes (Fig. SM1†).

In batch sorption experiments, a fixed adsorbent dose was agitated with 50 mL of adsorbate at a constant temperature and pH, and for specific time intervals (Fig. SM1†). The metal ion concentration was analyzed on an atomic absorption spectrometer (model Aanalyst 400, Perkin Elmer). Adsorption capacities were calculated using eqn (1).

$$q_e = \frac{(C_0 - C_e)}{W} \times V \quad (1)$$

here, q_e is the amount (mg g⁻¹) of metal adsorbed, C_0 (mg L⁻¹) and C_e (mg L⁻¹) are the initial and equilibrium metal concentrations, W is the adsorbent weight (g) and V (L) is the metal solution volume.

Kinetic and isotherm experiments were conducted to understand the thermodynamic adsorption behavior. A specific amount of adsorbent was added to 50 mL of adsorbate solution in the concentration range of 2–100 mg L⁻¹ at temperatures 25, 35 and 45 °C. Sorption equilibrium and dynamics data were fitted to various isotherm models and rate equations.

Column experiments provide necessary parameters for scaling up fixed-bed reactors. Flow rate, bed-height, column width, and breakthrough time were obtained through column adsorption (Fig. SM1†).

2.2.1. Sorption equilibrium models. Freundlich,⁴⁶ Langmuir,⁴⁷ Temkin,⁴⁸ Sips or Langmuir–Freundlich,⁴⁹ Redlich–Peterson,⁵⁰ Radke and Prausnitz,⁵¹ Toth,⁵² and Koble–Corrigan,⁵³ models were used to fit the equilibrium data obtained for lead and cadmium adsorption on KPP and MKPP. A detailed discussion of the isotherm models are given in Table SM1.†

2.2.2. Kinetic models

(a) *Pseudo-first-order model.* The pseudo-first-order model is given in eqn (2).^{5,54,55}

$$q_t = q_e(1 - e^{-k_1 t}) \quad (2)$$

here, k_1 is first-order rate constant (min⁻¹), q_e is adsorbate adsorbed per gram of adsorbent, and q_t is adsorbate adsorbed at time 't'.



(b) *Pseudo-second-order model.* Pseudo-second-order adsorption (eqn (3)) is greatly influenced by the number of active sites on adsorbent surface.^{8,55}

$$\frac{t}{q_t} = \frac{1}{k_2 q_e^2} + \frac{t}{q_e} \quad (3)$$

here, k_2 ($\text{g mg}^{-1} \text{ min}^{-1}$) is the pseudo-second order rate constant, q_e (mg g^{-1}) is the amount of adsorbate adsorbed at equilibrium, and q_t (mg g^{-1}) is the amount of adsorbate adsorbed at any time t .

2.3. Thermodynamic studies

The thermodynamic studies were performed at various Pb^{2+} and Cd^{2+} initial concentrations (10–100 mg L^{-1}) at 25, 35, and 45 °C. The thermodynamic parameters, ΔS° (entropy), ΔG° (Gibbs free energy) and ΔH° (enthalpy), were evaluated using the eqn (4)–(6).⁵⁶

$$\Delta G^\circ = -RT \ln b \quad (4)$$

$$\Delta H^\circ = R \left(\frac{T_1 T_2}{T_1 - T_2} \right) \ln \frac{b_1}{b_2} \quad (5)$$

$$\Delta S^\circ = \frac{\Delta H^\circ - \Delta G^\circ}{T} \quad (6)$$

where b , b_1 , b_2 are the constants the Langmuir constants at 25, 35, and 45 °C while R and T are the gas constant (8.314 $\text{J mol}^{-1} \text{ K}^{-1}$) and the absolute temperature, respectively.

2.4. Fixed-bed studies of Pb^{2+} removal and desorption

Adsorption isotherms are conventionally used for preliminary investigations and to know the operational parameters. However, it is essential to obtain a factual design model for practical applicability of biosorbents in column operations. A column (40.0 × 2.0 cm) was filled with KPP (30–50 B.S.S. mesh) with glass wool support (Fig. SM1†). The biosorbent (5 g) was slurried with hot water and fed slowly into the column to avoid air entrapment. The column was then loaded with the adsorbate (Pb^{2+}), which percolated downward with a flow rate of 5.0 mL min^{-1} . The bed height was 6.0 cm. The influent lead concentration and the solution pH were 10 mg L^{-1} and 4.5, respectively. Effluent samples were collected from the outlet of the column at different time intervals until the effluent lead concentration became nearly equal to the influent lead concentration. The adsorbent was regenerated using 0.1 N HCl by elution through the column as during the adsorption step.

2.5. Application of KPP and MKPP biosorbents in an actual groundwater sample

Actual wastewater is often a complex system of multiple ions. During Pb^{2+} and Cd^{2+} adsorption, these other ions can compete for adsorption sites. The ions may change the adsorption efficiency of an adsorbent. The effect of interfering ions on Pb^{2+} and Cd^{2+} adsorption was tested on a groundwater sample collected from Khekra, Baghpat district Uttar Pradesh, India at latitude 28°52'00" N, and longitude 77°17'00". This

groundwater sample was spiked with a concentration of 50 mg L^{-1} of both Pb^{2+} and Cd^{2+} solution. Adsorption studies were conducted at an adsorbent dose of 1 g L^{-1} (KPP) and 2 g L^{-1} (MKPP) at 25 °C for 24 h. After 24 h, the samples were filtered and analyzed for the concentrations of Na^+ , Ca^{2+} , and Mg^{2+} . The sample's conductivity was also measured after adsorption.

2.6. Application of magnetic and non-magnetic biosorbents in multicomponent adsorption of Pb^{2+} and Cd^{2+}

The adsorption capacity of MKPP and KPP for Pb^{2+} and Cd^{2+} from a multicomponent system containing more than one metal ion was examined in the batch mode. Adsorption experiments were conducted on equimolar ratios (1 : 1 : 1) of Pb^{2+} , Cd^{2+} and Cu^{2+} . The concentration range used was 2–100 mg L^{-1} . Test solutions were made at pH 4.5 for Pb^{2+} adsorption. Studies were conducted at 25 °C by adding 1 g L^{-1} of adsorbent to 50 mL of each test solution. All samples were agitated for 24 h. After that, all the equilibrium pH values were measured. Then the Pb^{2+} and Cd^{2+} concentrations were analyzed.

3. Results and discussion

3.1. Characterization of KPP and MKPP

The BET surface areas of KPP and MKPP were 1.8 $\text{m}^2 \text{ g}^{-1}$ and 52 $\text{m}^2 \text{ g}^{-1}$, respectively, *versus* cupuassu shell (1.2 $\text{m}^2 \text{ g}^{-1}$) [Fig. SM2(A and B)†].⁵⁷ The surface area of agricultural residues is usually low.⁵⁷ There was a sharp increase in surface area upon magnetization due to the presence of small bound iron oxide particles in MKPP [Fig. SM2(B)†]. The average pore diameter (BJH) of KPP and MKPP were 22.6 nm and 15.3 nm, respectively [Fig. SM3(A and B)†]. The average pore diameters of KPP and MKPP are mainly of the mesoporous type. The average pore volumes of KPP and MKPP were 0.01 $\text{cm}^3 \text{ g}^{-1}$ and 0.20 $\text{cm}^3 \text{ g}^{-1}$.

KPP and MKPP showed acidic pH_{PZC} values of 4.0 and 5.0, respectively [Fig. 2(a and b)]. Thus, KPP and MKPP have acidic surfaces with many oxygenated functional groups, including carboxylic acids, phenols, catechols, acidic alcohols, and enols on the biomass and surface Fe–OH groups on the iron oxide particles. The oxygen content was 40 and 32% for KPP and MKPP, respectively. Some of these oxygenated functional groups may form chelates with Pb^{2+} and Cd^{2+} .

Elemental analyses of KPP and MKPP showed the presence of traces of S, P, Cl, K, Ca, Cu, and Zn (Table 1). A small wt% of iron (4%) was estimated in MKPP while none appeared in KPP. This demonstrated successful loading of iron oxide on KPP (Table 1).

XRD was employed to identify crystalline phases in KPP and MKPP. The degree of crystallinity for biomass has been reported in the range of 13–17% and 20–23% is due to cellulosic polymorphs.^{58,59} The 20–23% degree of crystallinity occurs as a broad diffusion peak attributed to two cellulosic polymorphs, waxes and the complex nature of bonding between these structures.⁵⁸ X-ray diffraction of non-magnetic Kaniar pod powder (KPP) shows a broad peak ($2\theta = 22$) due to the cellulose(II) crystalline form [Fig. 3(a)]. The width of this peak may be ascribed to the presence of other organic matter such as lignin



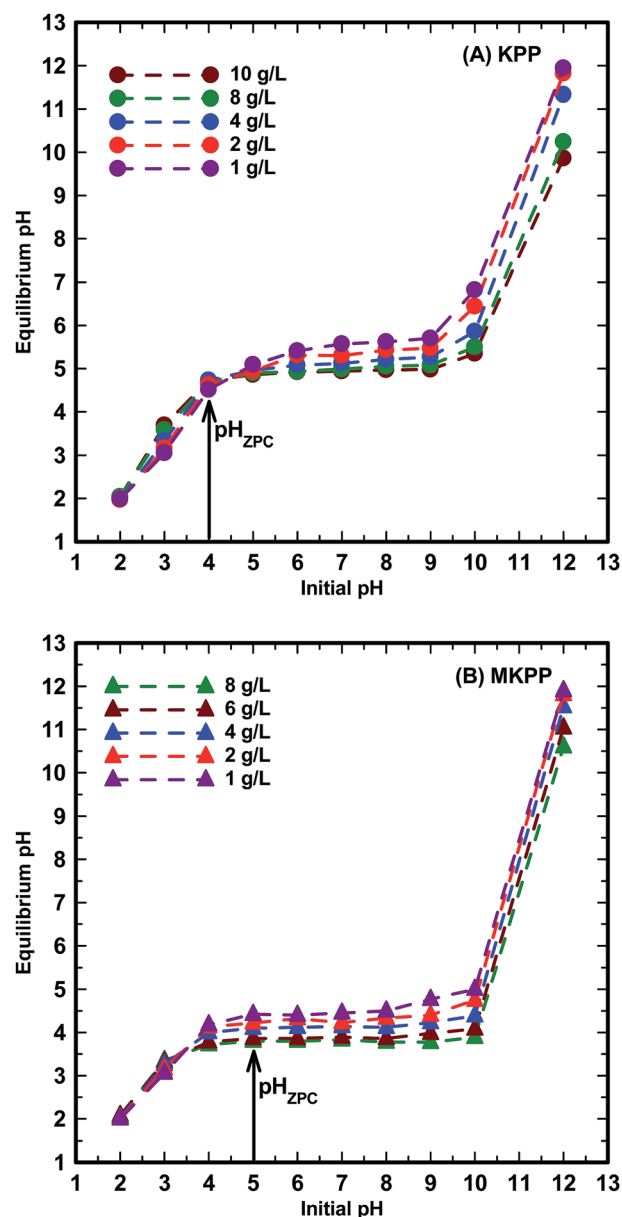


Fig. 2 Effect of adsorbent amount on the equilibrium pH of the water with no Pb^{2+} and Cd^{2+} concentration onto (A) KPP and (B) MKPP.

and hemicellulosic.^{58,60} The other peaks at $2\theta = 43.5^\circ$, 51.06° , 72.63° observed for this powder are assigned to cristobolite, quartz, and cristobolite quartz, respectively. The silica may be present both as cristobolite, and quartz. Other than silica, an intense calcite peak is also present at $2\theta = 72.63^\circ$.^{60,61} Most silicate mineral components of biomass contribute to the plant's rigidity and posture. Mineral introduction into the plants can take place through both natural and anthropogenic routes. Majority of transport in plants is routed from soil, where minerals are in abundance.⁵⁸ The iron oxide phase in MKPP, identified as magnetite (Fe_3O_4), has some intense iron oxide XRD peaks [Fig. 3(b)]. These characteristic magnetite peaks ($2\theta = 30.1$, 35.4 , 43.0 , 57.0 , and 62.5) and their indices [(220), (311), (400), (511), (440)] are observed in Fig. 3(b).

Table 1 Properties of non-magnetic Kanjar pod powders (KPP) and magnetic Kanjar pod powders (MKPP)

Properties	KPP	MKPP
Proximate analyses		
Moisture (wt%)	4.7	3.8
Ash (wt%)	0.06	12.5
Volatile (wt%)	49.6	44.6
Fixed carbon (wt%)	45.7	39.1
Water holding capacity (%)	44.5	52.9
Ultimate analyses		
C (wt%)	47.0	42.0
H (wt%)	6.3	5.5
N (wt%)	6.1	7.8
O (wt%)	40.6	32.3
Elemental analyses		
S (ppm)	181.4	1638
P (ppm)	108.1	838
Cl (ppm)	26.2	25.8
K (ppm)	37.7	5.9
Ca (ppm)	1961	1026
Cu (ppm)	10.6	18.4
Zn (ppm)	6.6	16.9
Fe (%)	—	4.02
Surface area characterization		
S_{BET} ($\text{m}^2 \text{g}^{-1}$)	1.8	52.0
V_{T} ($\text{cm}^3 \text{g}^{-1}$)	0.01	0.2
Bulk density ($\text{cm}^3 \text{g}^{-1}$)	0.18	—
pH_{PZC}	~ 4.0	~ 5.0

The other diffraction peak in KPP and MKPP near 30° is due to the presence of sulfate minerals. Another less intense peak, observed at 53.8° , corresponds to hematite.⁶² Hematite is also deposited in addition to magnetite in the magnetic biomass during the magnetization process. Use of iron sulfate during MKPP synthesis accounts for some hematite formation.⁵⁸ XRD confirms iron oxide deposition occurs on the KPP surfaces.⁶³

SEM micrographs of KPP and MKPP, before and after Pb^{2+} and Cd^{2+} adsorption, are shown in Fig. 4(A and B) and 5(A and B). KPP surfaces are rough, shiny and heterogeneous, with a rugged morphology [Fig. 4(A and B)]. This suggests potential for their Pb^{2+} and Cd^{2+} sorption within pores.⁶⁴ The morphology of MKPP was entirely different from KPP [Fig. 5(A and B)]. MKPP appeared brighter than KPP.⁶⁵ The cavernous openings seen for KPP in Fig. 4(B) appear to be smoothed over in MKPP (Fig. 5(B) and (C)). Nevertheless MKPP has the greater BET surface area.

Fig. 4(C–F) and 5(C–F) shows the spatial distribution of elements on KPP and MKPP, respectively, using SEM-EDX mapping. As seen in Fig. 4(D and F) and 5(D and F)], Cd^{2+} and Pb^{2+} are uniformly distributed over KPP and MKPP surfaces after their adsorption. However, surface Cd^{2+} and Pb^{2+} concentrations are greater on KPP than MKPP. This is evident by more dense yellow spots of Cd^{2+} and Pb^{2+} present on KPP than MKPP surfaces [Fig. 4(D and F) and 5(D and F)]. However, MKPP had more than 28 times as much BET measured surface area where adsorbed metal ions could be spread out on.



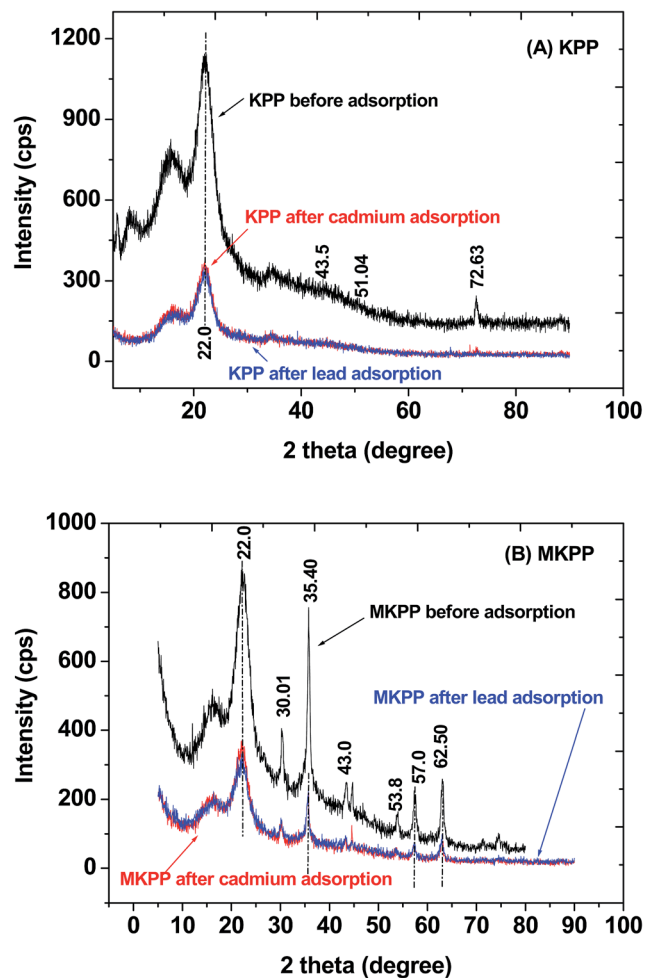


Fig. 3 XRD spectra of (A) Kaniar pod powder (KPP) and (B) magnetized Kaniar pods powder (MKPP) before and after Pb^{2+} and Cd^{2+} adsorption.

TEM micrographs of KPP are shown in Fig. 6(A). TEM and electron diffraction (ED) micrographs of MKPP are shown in Fig. 6(B–D). Fig. 6(C) inset shows the diffraction pattern obtained for MKPP. The lattice fringes of magnetite are also obtained [Fig. 6(D)]. The aggregation of MKPP primary particles may be due to the agglomerating tendency of the KPP portions of the exposed surfaces.⁶⁶ The high-resolution TEM (HRTEM) image of the selected area shows a highly crystalline character with a well ordered lattice. This lattice structure observed by HRTEM is consistent with the iron oxide peak position in the XRD pattern [Fig. 6(D)]. The corresponding selected area electron diffraction (SAED) pattern [inset of Fig. 6(C)] displays aggregated semispherical particles indicating this hybrid bio-composite's polycrystalline nature.⁶⁷

Fig. 7(A and B) shows FTIR spectra of KPP and MKPP before and after both Pb^{2+} and Cd^{2+} adsorption. KPP exhibited an intense broad band from about $3500\text{--}2700\text{ cm}^{-1}$ maximizing at 3421 cm^{-1} . This is due to the combination of isolated and hydrogen-bonded aliphatic, phenolic, and carboxylic acid O–H stretching bands.^{68,69} Both sp^2 C–H and sp^3 C–H stretching are buried in this envelop in the $3100\text{--}2800\text{ cm}^{-1}$ region.⁷⁰ Other

bands were observed at 2247 , 1751 , 1517 , 1271 , 1145 , 954 and 669 cm^{-1} . These correspond, respectively, to CO_2 at 2247 cm^{-1} , carbonyl stretching at 1751 cm^{-1} ,⁶⁵ sp^2 C–O stretching of carboxylic acids and esters (1271 cm^{-1}), ether and free alcohol sp^3 C–O stretching ($1000\text{--}1280\text{ cm}^{-1}$),⁵⁸ and out-of-plane H-deformations on substituted phenyl rings (669 cm^{-1}).⁷¹

Major FTIR peak shifts and disappearances were observed in the post-adsorption biosorbent samples. Peaks at 3568 , $3500\text{--}2800$, 2247 , 1517 , 1271 , 1145 , and 954 cm^{-1} disappeared and the quality of the spectra became very poor. New peaks at 2366 , 1631 , and 1558 cm^{-1} appeared after metal adsorption on KPP [Fig. 7(A and B)]. The decrease in free hydroxyl group intensity corresponds to Cd^{2+} coordination to carboxylic acid, phenolic and other possible sites. Smaller changes are observed in Fig. 7 after Pb^{2+} biosorption. The FTIR spectrum is consistent with Pb^{2+} coordination or chelation to carbonyl and other hydroxyl sites on the surface. The FTIR spectra of MKPP (pristine and loaded) exhibit the same before-to-after type changes upon sorption of Pb^{2+} and Cd^{2+} [Fig. 7(B)]. Iron oxide deposition alone on lowers the quality of the spectrum of the biostructure portion of the adsorbent. Coordination of Pb^{2+} and Cd^{2+} with carboxylic acids lowers the carbonyl stretching frequency and broadens this $1800\text{--}1700\text{ cm}^{-1}$ region. The fact these bands largely disappear in both Fig. 7(A and B) may correspond to this coordination.

The Raman spectra of pristine and loaded KPP and MKPP are shown in Fig. SM4(A and B).[†] KPP's Raman bands at 3174 , 3005 , and 2677 cm^{-1} are C–H stretching vibrations.⁷² sp^2 C–H (aromatic and olefin) stretching were observed at 3025 and 3006 cm^{-1} .⁷³ Peaks at 3174 and 3005 cm^{-1} in both KPP and MKPP were observed. The deformation vibration (scissoring mode) of the CH_2 group appears in the $1450\text{--}1480\text{ cm}^{-1}$ region.⁷⁴ The band at 1465 cm^{-1} in KPP and MKPP may be due to the CH_2 group. The bands observed from 950 to 1150 cm^{-1} are assigned to stretches of skeletal rings of cellulosic, hemicellulosic, lignin and glycosidic C–O and alcoholic C–O bonds.^{58,74}

After adsorption of Pb^{2+} and Cd^{2+} by KPP and MKPP, the FT-Raman spectra looked very similar to the spectra before adsorption. These spectra are not useful in trying to understand any specifics about the adsorption process at the surface.

The saturation magnetization (M_s) of the composite was investigated at 5 K and 300 K using a physical property measurement system (PPMS) with an applied field range of $-8000\text{ Oe} \leq H \leq 8000\text{ Oe}$ for quantitative confirmation of the adsorbent's magnetization. The magnetic hysteresis loop of MKPP is shown in Fig. 8. The MKPP sample is ferromagnetic. The M_s values were 5.98 emu g^{-1} and 8.38 emu g^{-1} at 300 K and 5 K , respectively. MKPP responded well when removed by a laboratory magnet from batch slurry adsorption experiments. The M_s values confirm convenient magnetic separations of exhausted adsorbent are possible from many media.

3.2. Effect of initial pH

The effect of pH on Pb^{2+} and Cd^{2+} adsorption onto KPP and MKPP is shown in Fig. 9(A and B). Adsorption of metals is a pH-dependent process as the surface charge and the metal speciation are both affected by the solution pH. The solution pH affects



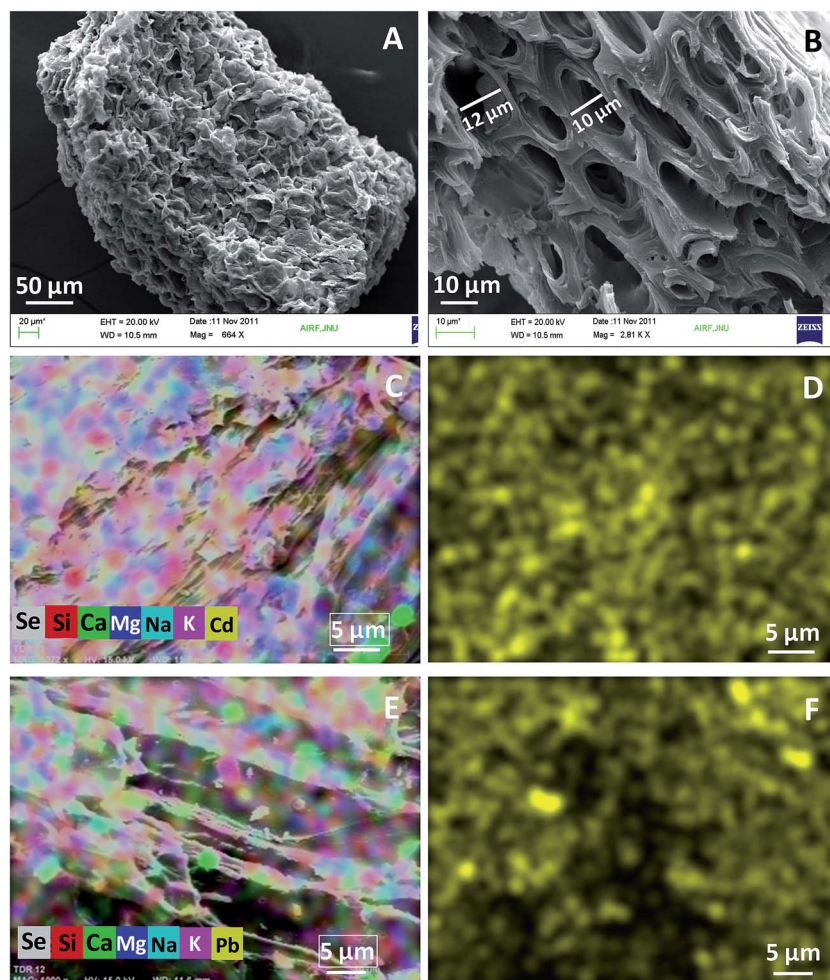
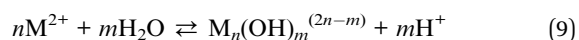
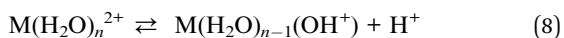
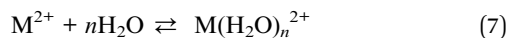


Fig. 4 SEM micrographs of Kanjar pod powder (KPP) at (A) 664 \times (B) 2.81k \times and SEM-mapping images of (C) multielements with Cd²⁺ and (D) Cd²⁺ (E) multielements with Pb²⁺ and (F) Pb²⁺ distribution.

the degree of dissociation of the carboxyl and hydroxyl functional groups of the adsorbent and the solubility of metal ions.^{75,76} Sorption of Pb²⁺ and Cd²⁺ on MKPP and KPP were restricted to the pH range from 2.0 to 6.0 to avoid metal ion precipitation. Lead and cadmium exist as Pb²⁺ and Cd²⁺ ions at pH 4.5 and 5.0, respectively.⁷⁶ Pb²⁺ and Cd²⁺ sorption increased significantly as pH increased from 2 to 4 and then modestly increased from 4.0 to 6.0. The Pb²⁺ and Cd²⁺ ions may undergo solvation, hydrolysis and polymerization to insoluble hydroxide/oxide species at pH 7.0, where precipitation can ensue (eqn (7)–(9)).⁵



The pH dependent adsorption of Pb²⁺ and Cd²⁺ between 2 to 6 occurs due to progressive deprotonation of KPP and MKPP surfaces. At pH 2.0, the biomass surface is positively charged and repels Pb²⁺ and Cd²⁺, resulting in low metal uptake.⁷⁷ As

pH raises, carboxylic acids, enols, and acidic alcohols on the adsorbent loose protons, and the surface becomes more negatively charged. This attracts and binds Pb²⁺ and Cd²⁺. As negative charge density increases at the surface, more Pb²⁺ and Cd²⁺ are adsorbed. Carboxylic acids are most acidic and lose protons first, followed by acidic alcohol sites. At higher pH, phenols are increasing converted to phenoxide sites, but this effect will occur most strongly from pH 7.5–10.0, beyond the pH range studied. In MKPP, magnetite surfaces contain Fe–OH groups. These groups also deprotonate progressively as pH rises or increasingly protonate at low pH. Thus, varying solution pH biases both surface charging and attraction or repulsion of Pb²⁺ and Cd²⁺ of the magnetic surface similar to the biological cell walls of KPP. The individual functional group protonation/deprotonation equilibria are all occurring as a function of solution pH and within the surface-wide context of the pH_{ZPC}, which have values of 5.0 for KPP and 4.0 for MKPP [Fig. 2(A and B)].

Maximum Pb²⁺ and Cd²⁺ removal occurred at pH 4.5 and 5.0 for KPP and MKPP, respectively [Fig. 9(A and B)]. At a metal concentration of 10 mg L^{−1} and a 2 g L^{−1} adsorbent dose, Pb²⁺ removal increased from 24 to 98% for KPP and 13 to 83% for



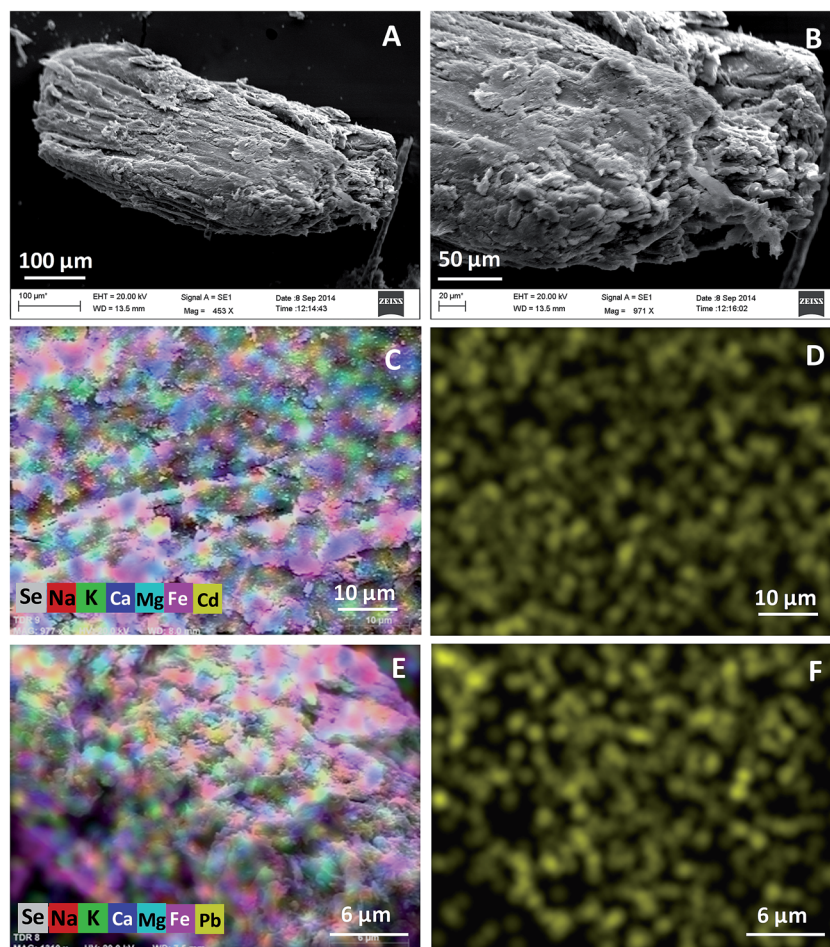


Fig. 5 SEM micrographs of magnetic Kanjar pod powder (MKPP) at (A) 664 \times (B) 2.81k \times and SEM-mapping images of (C) multielements with Cd^{2+} and (D) Cd^{2+} (E) multielements with Pb^{2+} and (F) Pb^{2+} distribution.

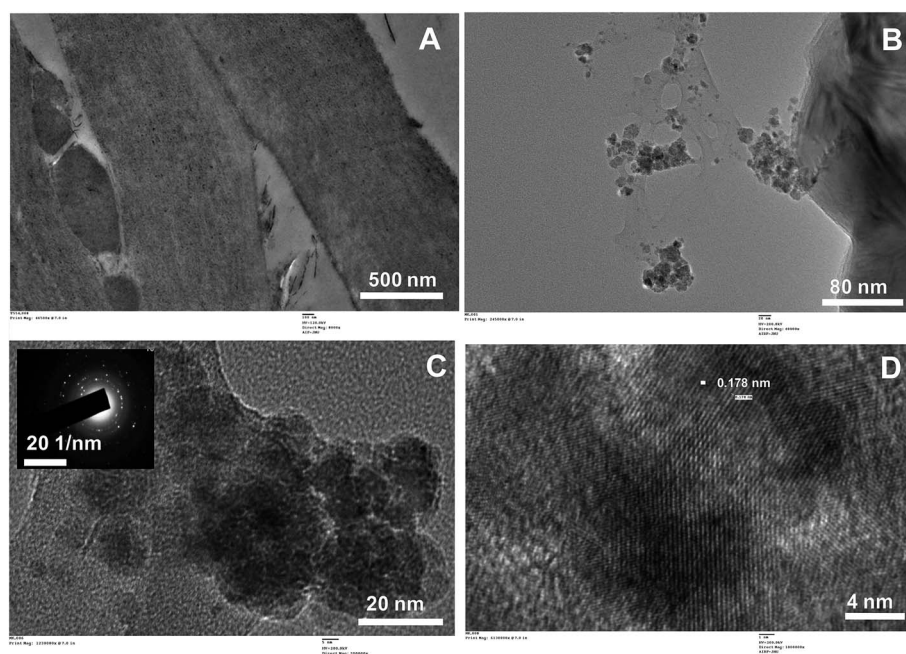


Fig. 6 TEM micrographs of (A) Kanjar pods powder (KPP) and (B–D) magnetic Kanjar pods powder (MKPP) at different magnifications. The inset in the upper left (C) is a SAED pattern and (D) HRTEM micrograph.



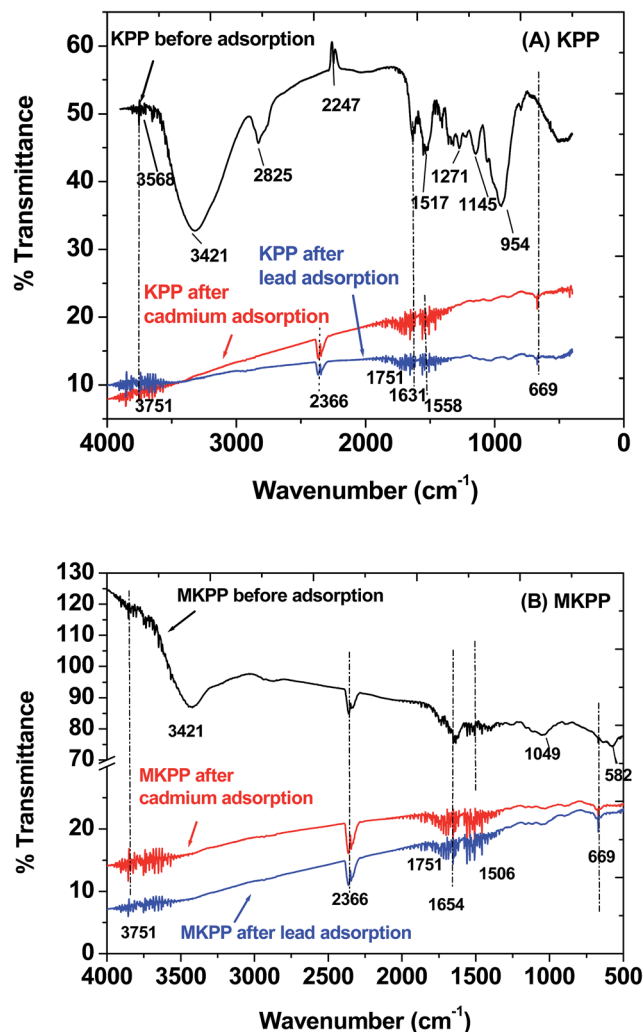


Fig. 7 FTIR spectra of (A) KPP and (B) MKPP before and after Pb^{2+} and Cd^{2+} adsorption.

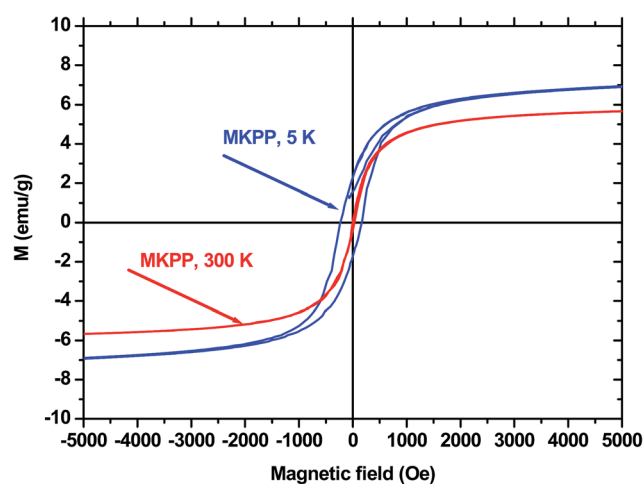


Fig. 8 Magnetic moment of magnetic Kanjar pod powder (MKPP) at 5 K and 300 K.

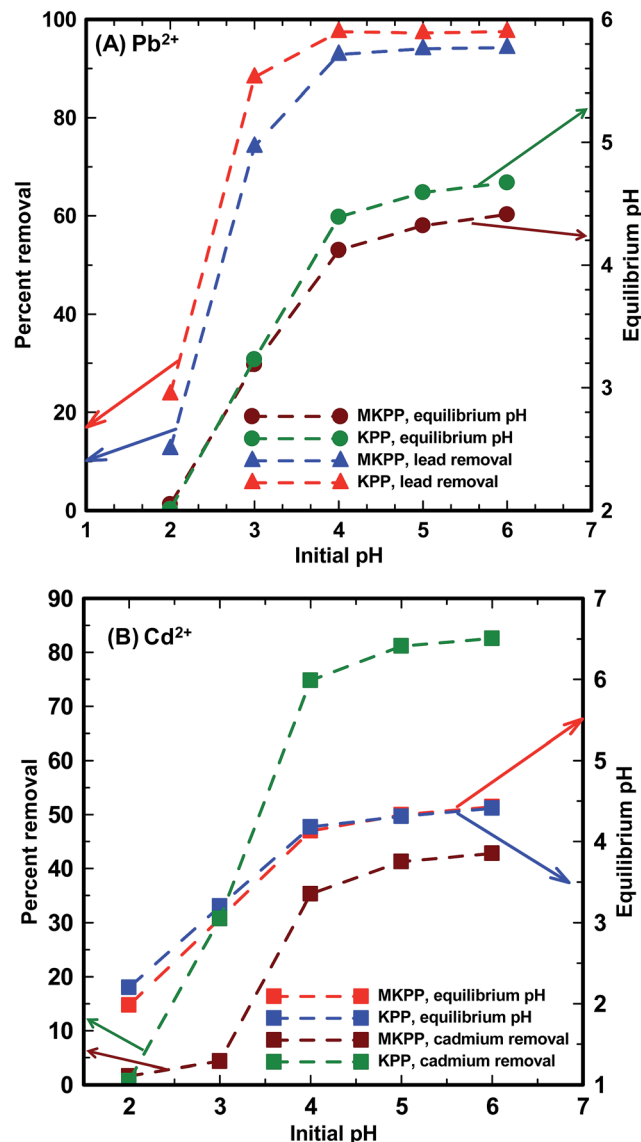


Fig. 9 Effect of pH on (A) Pb^{2+} and (B) Cd^{2+} removal by KPP and MKPP [initial Pb^{2+} and Cd^{2+} concentration = 10 mg L^{-1} ; adsorbent dose = 2 g L^{-1} ; particle size = 30–50 B.S.S. mesh; $T = 25^\circ \text{C}$].

MKPP when pH rose from 2.0 to 6.0. Similarly, Cd^{2+} removal went up from 1 to 83% using KPP and 2 to 43% using MKPP upon increasing the initial pH from 2.0 to 6.0. Above the adsorbents' pH_{PZC} the surface is negatively charged. Here, much more metal adsorption was observed. When KPP and MKPP was used to adsorb Pb^{2+} and Cd^{2+} at $\text{pH} > \text{pH}_{\text{PZC}}$, the solution equilibrium pH dropped. This occurs because deprotonation of the adsorbent's acidic functional groups releases H_3O^+ as metal cations are adsorbed.^{5,8} Therefore, all the kinetic and equilibrium sorption experiments were carried out at pH 4.5 and 5.0.

3.3. Cd^{2+} and Pb^{2+} sorption mechanism

Agricultural crop residues contain cellulose, lignin, lipids, proteins, simple sugars, starches, functional group-rich compounds that can bind heavy metals.⁷⁸ Specifically, seed pods constituting KPP and MKPP contain a rich variety of secondary metabolite compounds



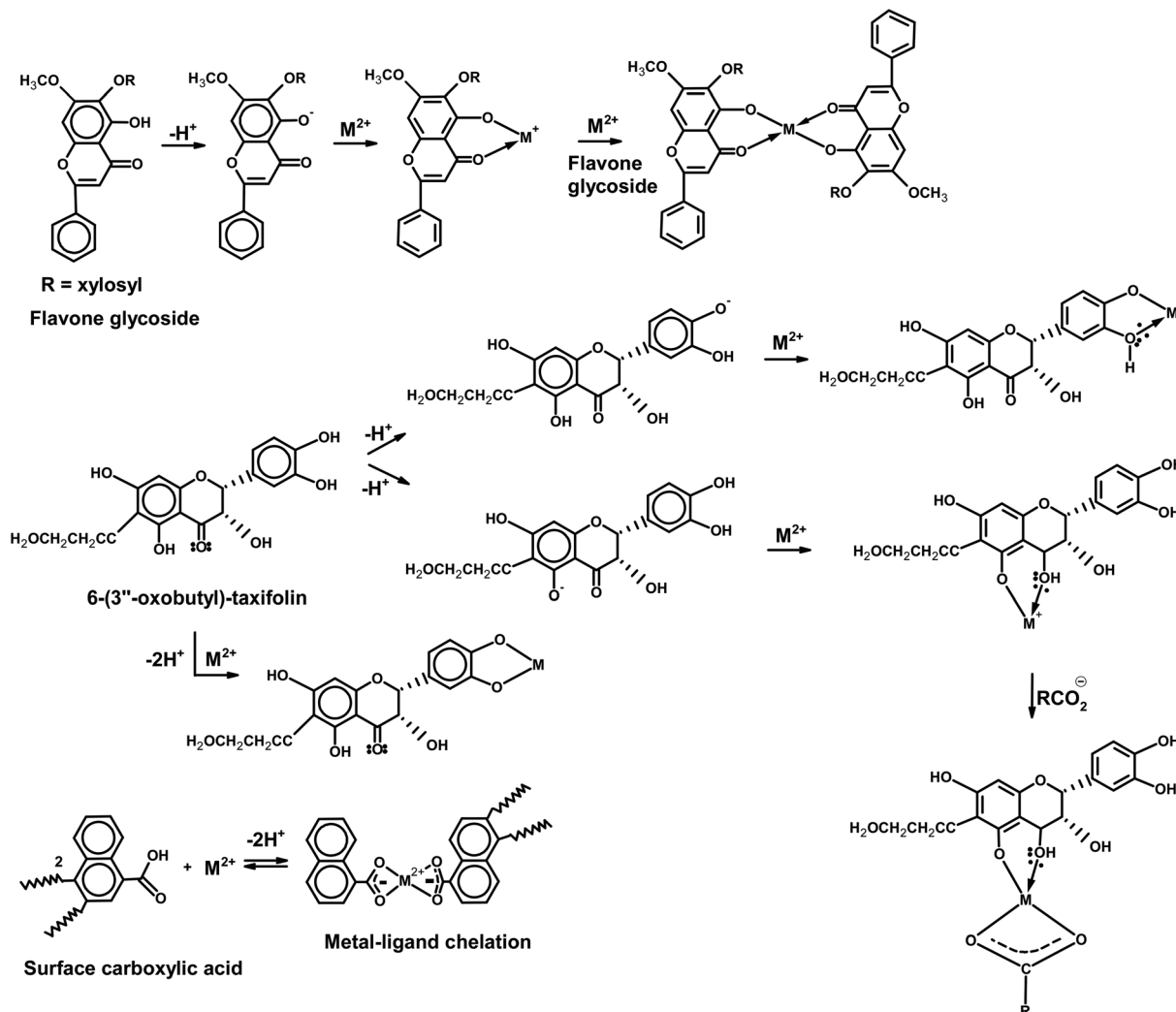


Fig. 10 Example Pb^{2+} and Cd^{2+} sorption complexes possible to representative chelating compounds present in KPP and MKPP.

including glycosides, flavenoids, phenolic compounds, oxepins, fatty acids and phytosterols.⁷⁹ We thought these would uniquely contribute to metal chelation and sorption. Previously, mechanisms have been proposed for aqueous Pb^{2+} and Cd^{2+} remediation,^{4,5,80} which included electrostatic attraction–repulsion interactions, ion exchange, functional group–metal complex formation, H-bonding, and chelation.⁸¹ The presence of so many components in *Bauhinia purpurea* which can chelate metals has focused our attention on the compounds which have been

identified in this species as example adsorbents.⁷⁹ Fig. 10 shows two of these more unique specific compounds from *Bauhinia purpurea* and a surface carboxylic acid as sample adsorption site for either Pb^{2+} or Cd^{2+} . Of course many other specific adsorption sites exist.

Chelation of M^{2+} ions are shown by several functions in Fig. 10. *o*-Keto phenol functions in both the xylosyl flavone and taxifolin can singly or doubly chelate M^{2+} ions with the release of protons to solution. Likewise, the catechol function (shown here

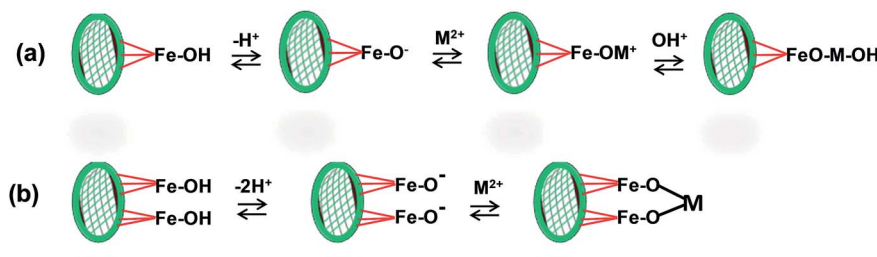


Fig. 11 Adsorption mechanism for Pb^{2+} and Cd^{2+} adsorption by MKPP.





Table 2 Pseudo-first-order and pseudo-second-order rate constants and comparative evaluation of experimental q_e values with their corresponding values obtained using first- and second-order rate equations at different adsorbent dosages and adsorbate concentrations

Values		First order rate constant, k_1 (h^{-1})		Second order rate constant, k_2 ($\text{mg g}^{-1} \text{h}^{-1}$)		Second order rate constant, k_2 ($\text{mg g}^{-1} \text{h}^{-1}$)		q_e experimental (mg g^{-1})		q_e calculated using first order kinetic model (mg g^{-1})		q_e calculated using second order kinetic model (mg g^{-1})	
KPP	MKPP	KPP	R^2	KPP	R^2	KPP	R^2	KPP	MKPP	KPP	MKPP	KPP	MKPP
At different adsorbent dose (g L^{-1}), Pb^{2+}													
0.5	0.5	0.18	0.52	0.078	0.85	0.12	0.99	0.064	0.99	17.24	15.56	3.39	4.84
1	2	0.24	0.62	0.140	0.93	0.35	0.99	0.17	0.99	9.08	4.46	1.74	2.13
4	4	0.15	0.45	0.108	0.43	4.45	1	1.38	0.99	2.32	2.07	0.11	0.270
At different adsorbent dose (g L^{-1}), Cd^{2+}													
0.5	1	0.047	0.04	0.009	0.00	0.2	0.98	0.903	0.99	14.84	3.12	1.52	0.71
1	2	0.085	0.09	0.067	0.29	0.45	0.99	0.282	0.99	10.70	4.47	1.36	0.65
2	4	0.023	0.02	0.157	0.52	0.85	0.99	0.238	0.98	7.28	3.70	0.62	1.23
At different Pb^{2+} concentrations (mg L^{-1})													
10		0.140	0.31	0.099	0.23	0.48	0.99	0.48	0.99	8.82	4.09	0.90	0.67
20		0.898	0.61	0.075	0.34	0.12	0.99	0.22	0.99	16.94	7.42	3.40	1.70
50		0.108	0.49	0.085	0.51	0.09	0.99	0.14	0.99	27.89	14.54	4.18	2.97
At different Cd^{2+} concentrations (mg L^{-1})													
10		0.122	0.74	-0.087	0.11	0.213	0.99	0.35	0.92	7.47	4.22	2.17	0.71
30		0.163	0.78	-0.030	0.11	0.094	0.99	0.85	0.98	16.18	7.38	4.42	0.64
60		0.057	0.28	-0.009	0.03	—	0.99	0.72	0.99	22.59	9.74	1.97	1.24

in taxifolin) can chelate to bind either M^{2+} to generate M^+ or further to neutral complexes. Alternatively, a single carboxylate can combine with another chelating function to immobilize to metal. Metal–ligand chelation by oxygens is the major interaction in the 4.5–5.0 pH range.⁸¹ A possible mechanism for M^{2+} on the magnetite portion of MKPP is shown in Fig. 11, where surface Fe–OH or Fe–O– sites actively bind Cd^{2+} and Pb^{2+} ions.

3.4. Pb^{2+} and Cd^{2+} sorption dynamics

The Pb^{2+} and Cd^{2+} sorption efficiency as a function of biomass dosage was investigated. Fig. SM5 and SM6† show the effect of sorbent dose on Pb^{2+} and Cd^{2+} removal. Both Pb^{2+} and Cd^{2+} uptake increased at higher adsorbent dose, because more adsorption sites were available. A significant jump in Cd^{2+} removal was observed on increasing KPP dose from 0.5 to 1.0 g L^{-1} . No further uptake occurred on introducing an additional 1.0 g L^{-1} of KPP (Fig. SM6†). Similar behavior was observed for MKPP (Fig. SM6†). The maximum sorption percentage achieved by KPP and MKPP reached 96% and 79%, respectively for $Cd(II)$ at a biomass concentration of 0.5 g L^{-1} . Therefore, 1.0 and 2.0 g L^{-1} dosage amounts were selected for KPP and MKPP, respectively in all subsequent equilibrium and dynamic experiments. Pb^{2+} sorption studies were carried out at 0.1, 1.0 and 4.0 g L^{-1} dosages for KPP and MKPP. Dosage of 1.0 and 2.0 g L^{-1} resulted in 96% and 97% Pb^{2+} removal by KPP and MKPP, respectively. Further dose increments did not show any further significant uptake. Thus, all dynamic and equilibrium studies were performed at 1.0 and 2.0 g L^{-1} dosage for KPP and MKPP, respectively. The effect of initial Cd^{2+} and Pb^{2+} concentrations were investigated (Cd^{2+} : 10, 20 and 50 mg L^{-1} ; Pb^{2+} : 10, 30 and 60 mg L^{-1}). Cd^{2+} and Pb^{2+} removal increased on increasing initial adsorbate concentrations, due to the availability of more adsorbate ions and their higher concentrations [Fig. SM7 and SM8†]. The effect of temperature was also investigated [Fig. SM9 and SM10†].

Sorption dynamics data were fitted to pseudo-first-order⁵⁴ and second-order⁵⁵ equations (Fig. SM11–SM14† and Table 2). The pseudo-second-order equation best fit the dynamics data at various adsorbent dosages and initial metal concentrations. Higher correlation coefficients (>0.99) were obtained using the second-order equation (Table 2). Experimental ' q_e ' values were similar to theoretical ' q_e ' values obtained using pseudo-first-order equation (Table 2). Similar results were reported for $Pb(II)$ ⁸² and $Zn(II)$ biosorption.⁸³ Therefore, chemisorption was the rate determining step for Cd^{2+} and Pb^{2+} removal by KPP and MKPP.

3.5. Pb^{2+} and Cd^{2+} sorption equilibrium

Sorption equilibrium studies were conducted at 25°, 35° and 45 °C for Cd^{2+} (initial pH = 4.5) and Pb^{2+} (initial pH = 5.0) [Fig. 12 and 13]. The initial Cd^{2+} and Pb^{2+} concentration range was 2–100 mg L^{-1} and equilibrium time was 24 h [Fig. 13 and 14]. Sorption equilibrium data were fitted to Langmuir [Fig. 12 and 13],⁴⁷ Freundlich,⁴⁶ Redlich–Peterson,⁵⁰ Radke–Prausnitz,⁵¹ Toth,⁵² Koble–Corrigan,⁵³ Sips,⁴⁹ and Temkin⁴⁸ equations (Table

SM1†) using MATLAB (non-linear least square method) (Fig. SM15–SM18†).

Cd^{2+} uptake decreased with a temperature rise, whereas Pb^{2+} removal was generally unaltered by temperature. The Langmuir adsorption isotherm^{47,84} equation described Pb^{2+} and Cd^{2+} sorption on both KPP and MKPP, respectively, better than other isotherms. The Langmuir model had high R^2 [Fig. 12 and 13]. Moreover, Langmuir isotherms were also used to determine a dimensionless constant separation factor R_L [$R_L = 1/(1 + bC_0)$; $R_L > 1$ unfavorable; $R_L = 1$ linear; $0 < R_L < 1$ favorable and $R_L = 0$ irreversible]. R_L predicts whether the adsorption is favorable and unfavorable.^{85,86} The R_L values lie between 0 and 1 indicating that Pb^{2+} and Cd^{2+} adsorption on both KPP and MKPP is favorable.

The nonlinear Freundlich adsorption isotherms are given in Fig. SM15 and SM17† while the parameters are reported in Table 3. The $1/n$ values obtained for Pb^{2+} and Cd^{2+} adsorption on KPP and MKPP were between 0.1 and 0.5, indicating favorable adsorption. Among the three parameter equations, the Sips model best fitted (high R^2) the Pb^{2+} sorption data on KPP and MKPP (Table 3). Therefore, Pb^{2+} adsorption on KPP and MKPP

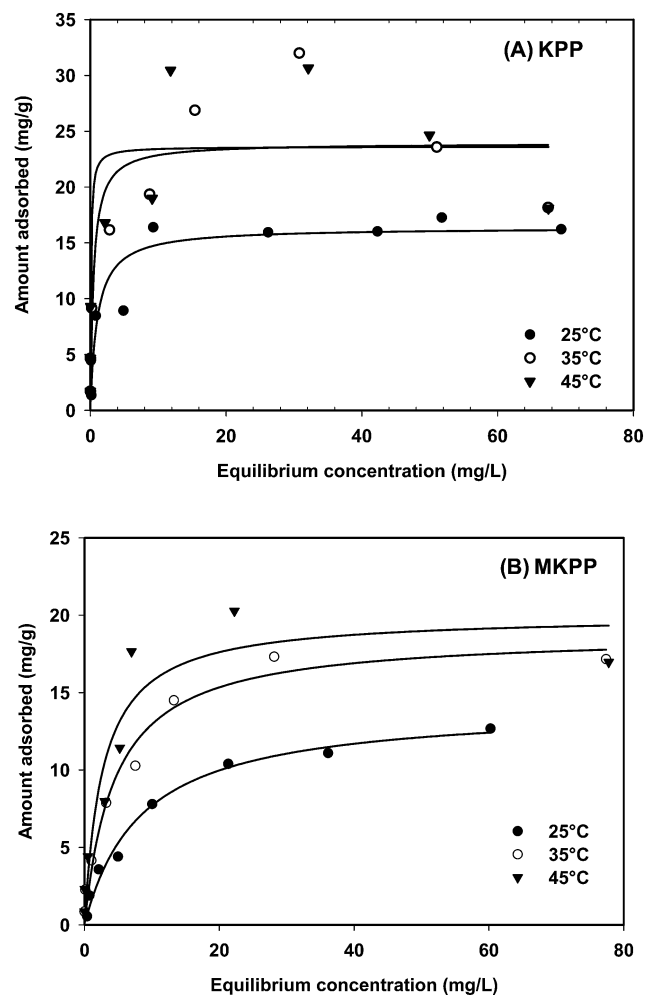


Fig. 12 Langmuir adsorption isotherm of Pb^{2+} on (A) KPP and (B) MKPP at 25, 35, 45 °C [pH = 4.5; initial Pb^{2+} concentration range = 2–100 mg L^{-1} ; $T = 25$ °C; adsorbent dose = 1 g L^{-1} (KPP) and 2 g L^{-1} (MKPP); particle size = 30–50 B.S.S. mesh].



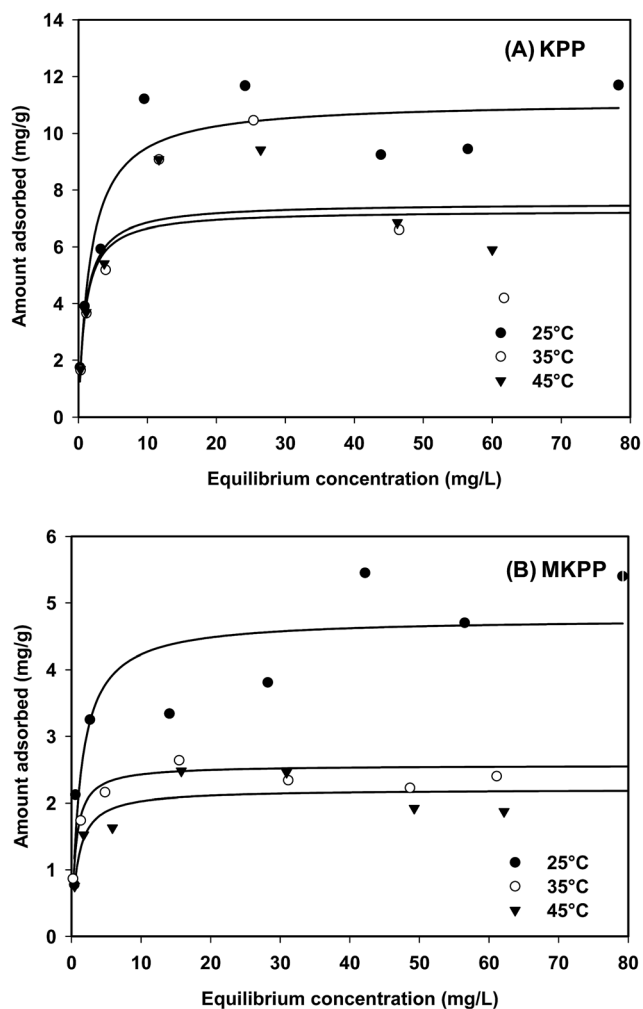


Fig. 13 Langmuir adsorption isotherm of Cd^{2+} by (A) KPP and (B) MKPP at 25, 35, 45 °C [pH = 5.0; initial Cd^{2+} concentration range = 2–100 mg L^{-1} ; $T = 25^\circ\text{C}$; adsorbent dose = 1 g L^{-1} (KPP) and 2 g L^{-1} (MKPP), particle size = 30–50 B.S.S. mesh].

was diffusion controlled at low metal-ion concentrations and followed monomolecular adsorption at high concentrations.⁵ Sorption data were also fitted to Redlich–Peterson and Radke–Prausnitz equations (Table 3).

3.6. Thermodynamics behavior

Studies performed at different temperatures are presented in Fig. 12 and 13.

The amount of Pb^{2+} adsorption onto both KPP and MKPP increases with a rise in temperature. Cd^{2+} adsorptions onto KPP and MKPP exhibit the opposite behavior as adsorption diminishes with an increase in temperature. All four processes are spontaneous. ΔG° is negative for Pb^{2+} and Cd^{2+} adsorption onto both KPP and MKPP and the thermodynamic parameters are given in Table 4. ΔH° is positive for Pb^{2+} adsorption on KPP and MKPP, confirming the endothermic nature, while the negative ΔH° obtained for Cd^{2+} adsorption on KPP and MKPP confirming exothermic nature. Positive ΔS° values for both Pb^{2+} and Cd^{2+} adsorption on KPP and MKPP suggested an increase

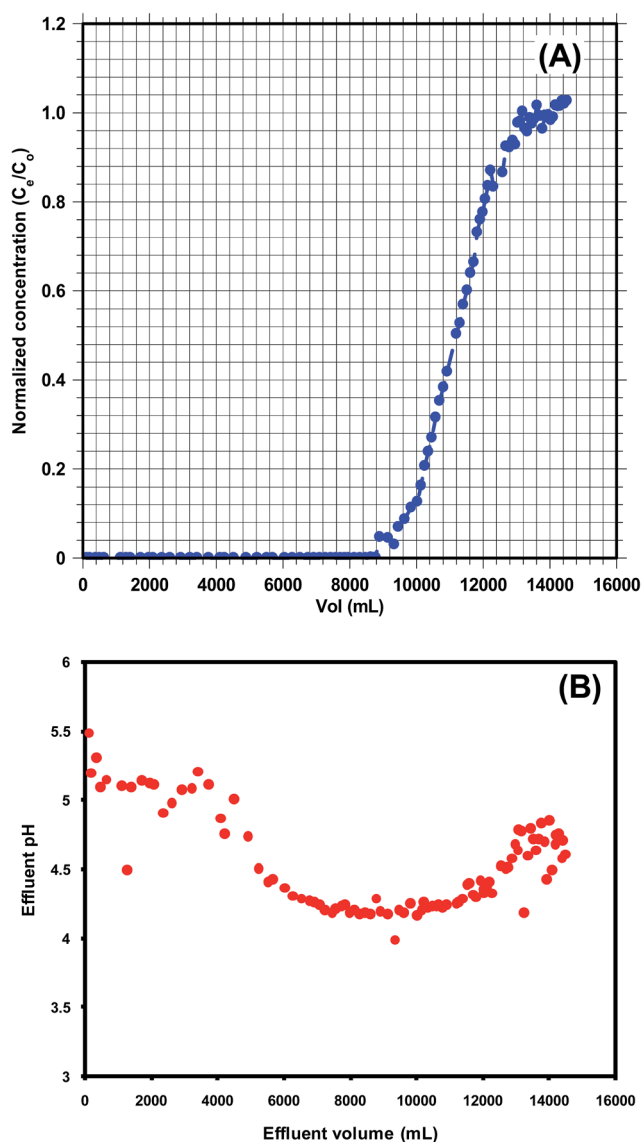


Fig. 14 (A) KPP breakthrough curve (particle size = 30–50 B.S.S. mesh, Pb^{2+} concentration = 10 mg L^{-1} , initial pH = 4.5) and (B) effluent pH curve for Pb^{2+} adsorption by KPP.

randomness with some structural or solvation changes occurring at solid/liquid interface.⁵⁶

3.7. Cd^{2+} and Pb^{2+} sorption in a multicomponent system

Adsorption in multi-component systems is a complex process. Therefore, simultaneous adsorption of Pb^{2+} , Cu^{2+} , and Cd^{2+} was carried-out in a ternary system. Adsorption isotherms were obtained at pH 4.5 (KPP) and 5.0 (MKPP) at 25 °C over a concentration range of 5–150 mg L^{-1} using a $\text{Pb}^{2+} : \text{Cu}^{2+} : \text{Cd}^{2+}$ ratio of 1 : 1 : 1. The percent Pb^{2+} and Cd^{2+} removal for KPP and MKPP, respectively, in the ternary system is shown in Fig. SM19 and SM20.† A Pb^{2+} removal of 20% to 80% and 15 to 50% for KPP and MKPP was observed, respectively [Fig. SM19 and SM20(A and B)†]. Obviously, the presence of both Cu^{2+} and Cd^{2+} interfere in Pb^{2+} adsorption. A similar trend was observed for Cd^{2+} (10–



Table 3 Sorption isotherm parameters for Pb²⁺ and Cd²⁺ adsorption from water on KPP and MKPP at different temperatures

Isotherm parameters	Pb ²⁺						Cd ²⁺					
	KPP			MKPP			KPP			MKPP		
	25 °C	35 °C	45 °C	25 °C	35 °C	45 °C	25 °C	35 °C	45 °C	25 °C	35 °C	45 °C
Freundlich												
K_F (mg g ⁻¹)	7.61	15.20	16.78	1.99	1.50	1.30	4.94	4.38	4.34	1.99	1.52	1.31
$1/n$	0.21	0.13	0.10	0.23	0.14	0.13	0.20	0.12	0.13	0.22	0.13	0.13
R^2	0.85	0.76	0.74	0.86	0.76	0.59	0.74	0.25	0.40	0.87	0.75	0.59
Langmuir												
Q^0 (mg g ⁻¹)	16.37	23.94	23.61	14.14	18.81	20.01	11.13	7.28	7.54	4.76	2.56	2.20
b	0.97	2.10	11.11	0.12	0.22	0.37	0.58	1.04	1.00	0.78	1.76	1.13
R^2	0.92	0.78	0.76	0.98	0.97	0.90	0.89	0.50	0.69	0.81	0.81	0.78
Sips												
K_{LF} (L g ⁻¹)	13.20	34.04	54.03	2.09	5.21	5.98	6.24	6.85	6.99	1.93	4.73	2.56
a_{LF} (L mg ⁻¹) a_{LF}	0.49	1.52	4.28	0.08	0.18	0.35	0.58	0.97	0.96	1×10^3	2.15	1.12
n_{LF}	0.56	0.62	0.49	0.83	0.81	1.15	1.06	1.39	1.31	0.28	0.86	1.04
R^2	0.90	0.80	0.78	0.98	0.97	0.90	0.88	0.52	0.70	0.86	0.91	0.77
Redlich–Peterson												
K_{RP} (L g ⁻¹)	39.68	5.87	10.30	2.21	3.96	3.48	4.16	1.65	2.29	9.60	6.95	2.05
a_{RP} (L mg ⁻¹) β_{RP}	3.67	0.06	0.18	0.24	0.19	0.04	0.22	0.01	0.05	3.73	3.32	0.81
β_{RP}	0.89	1.34	1.21	0.89	1.02	1.35	1.12	1.70	1.43	0.83	0.94	1.03
R^2	0.89	0.79	0.75	0.98	0.97	0.94	0.90	0.80	0.89	0.88	0.84	0.79
Temkin												
b_{Te} (J mol ⁻¹)	1.15	0.96	1.20	3.42	189.50	146.45	1.53	3.20	2.99	3.43	8.91	10.67
a_{Te} (L mg ⁻¹)	47.00	260.68	2135.41	16.14	8.90	10.67	17.41	146.91	90.23	16.15	189.49	146.45
R^2	0.89	0.78	0.76	0.87	0.79	0.65	0.82	0.31	0.49	0.87	0.80	0.65
Koble–Corrigan												
A_{KC}	13.2	34.0	53.97	2.13	5.20	5.79	6.24	6.87	6.98	2.35	3.75	2.50
B_{KC}	0.68	1.30	2.02	0.14	0.25	0.29	0.56	0.96	0.94	0.19	1.39	1.13
n_{KC}	0.56	0.62	0.48	0.83	0.81	1.16	1.06	1.36	1.30	0.31	0.71	1.01
R^2	0.90	0.80	0.78	0.98	0.97	0.88	0.89	0.51	0.70	0.87	0.83	0.78
Toth												
K_T	15.89	50.31	262.20	1.70	4.17	5.14	6.45	7.63	7.56	3.74	4.52	2.50
B_T	0.97	2.10	11.11	0.12	0.22	0.20	0.58	1.05	1.00	0.78	1.76	1.13
β_T	−6.49	−126.2	−68.77	0.52	0.35	0.23	0.59	0.19	0.92	0.11	0.71	0.52
R^2	0.86	0.78	0.76	0.98	0.96	0.90	0.89	0.50	0.69	0.81	0.82	0.78
Radke and Prausnitz												
A (L g ⁻¹)	39.68	76.28	361.60	2.20	1.46×10^4	7.66	4.16	1.65	2.29	9.60	6.90	2.05
b ((mg ^{1-β} L ^{β}) g ⁻¹)	10.82	20.65	20.45	9.09	4.18	19.20	18.41	112.60	41.37	2.57	2.09	2.53
β	0.11	0.04	0.05	0.10	0.36	0.01	−0.13	−0.70	−0.43	0.16	0.05	−0.03
R^2	0.89	0.79	0.77	0.98	0.87	0.90	0.90	0.80	0.89	0.88	0.84	0.79

Table 4 Thermodynamic parameters for Pb²⁺ and Cd²⁺ adsorption on KPP and MKPP

Metal ions	KPP					MKPP				
	ΔG° (kJ mol ⁻¹)			ΔH° (kJ mol ⁻¹)	ΔS° (kJ mol ⁻¹ K ⁻¹)	ΔG° (kJ mol ⁻¹)			ΔH° (kJ mol ⁻¹)	ΔS° (kJ mol ⁻¹ K ⁻¹)
	25 °C	35 °C	45 °C			25 °C	35 °C	45 °C		
Pb ²⁺	−34.2	−37.3	−42.9	59.1	0.31	−29.0	−31.5	−33.9	46.9	0.25
Cd ²⁺	−32.9	−35.4	−36.6	−3.6	0.10	−33.6	−36.8	−36.9	−35.9	0.003



Table 5 Pb^{2+} and Cd^{2+} removal from contaminated groundwater sample using KPP and MKPP (adsorbent dose 1.0 g L^{-1} (KPP) and 2.0 g L^{-1} (MKPP), equilibrium time 48 h; pH 4.5 (Pb^{2+}) and 5.0 (Cd^{2+}); temperature 25°C)

Parameters	Pb^{2+}			Cd^{2+}		
	Initial concentration	Concentration after treatment with KPP	Concentration after treatment with MKPP	Initial concentration	Concentration after treatment with KPP	Concentration after treatment with MKPP
Pb^{2+} (mg L^{-1})	42.81	31.24	27.81	—	—	—
Cd^{2+} (mg L^{-1})	—	—	—	48.65	38.24	37.36
Initial pH	4.5	4.57	3.96	5	5.21	3.99
Conductivity (ms cm^{-1})	3.54	3.46	3.55	1045	1070	1091
Salinity (ppt)	1.8	1.8	1.9	0.5	0.5	0.5
TDS (mg L^{-1})	1683	1706	1746	514	526	535
Na^+ (mg L^{-1})	69.9	56.1	66.5	66.7	13.8	15.3
K^+ (mg L^{-1})	3.5	2.9	2.9	2.7	0.1	0.2
Ca^{2+} (mg L^{-1})	16.68	16.7	20	17.56	8.2	8
Mg^{2+} (mg L^{-1})	50.05	48.6	48.93	50.03	49.59	48.93
Iron (mg L^{-1})	0.025	0.045	0.672	0.013	0.024	0.782

90% for KPP and 10–80% for MKPP [Fig. SM19 and SM20(A and B)]. More interference was observed for Cd^{2+} adsorption for this ternary system in the high concentration range. Overall, copper is expected to compete vigorously with both Pb^{2+} and Cd^{2+} for adsorption sites. It exhibits similar columbic responses and four-coordinate complexation chemistries with Pb^{2+} and Cd^{2+} .

3.8. Pb^{2+} and Cd^{2+} removal from actual groundwater

Natural water systems contain a complex mixture of ions. These may also interfere with Pb^{2+} or Cd^{2+} during adsorption on KPP and MKPP. Thus, Pb^{2+} or Cd^{2+} removal from groundwater samples, collected from Khekra Village, Baghpat District, Uttar Pradesh, India, by KPP and MKPP was investigated. The physicochemical characteristics of this groundwater are shown in Table 5. An additional 50 mg L^{-1} of either Cd^{2+} or Pb^{2+} was spiked into this water sample. Initial pHs were adjusted to 4.5 and 5.0 for Pb^{2+} and Cd^{2+} , respectively. A predetermined dose of KPP (1 g L^{-1}) or MKPP (2 g L^{-1}) was added to each sample. After 48 h, the samples were filtered and the Cd^{2+} and Pb^{2+}

Table 6 Fixed bed parameters for Pb^{2+} adsorption by KPP

Parameters	Values
C_0 (mg mL^{-1})	0.00822
C_x (mg mL^{-1})	0.00793
C_b (mg mL^{-1})	0.00026
V_x (mg cm^{-2})	33.36
V_b (mg cm^{-2})	0.74
F_m ($\text{mg cm}^{-2} \text{ min}^{-1}$)	0.01
D (cm)	6
t_x (min)	3092
t_b (min)	3023
t_b (min)	2216
F	0.27
δ (cm)	1.7
Saturation (%)	79.23
Usage rate (kg L^{-1})	0.0005
EBCT (min)	5.56

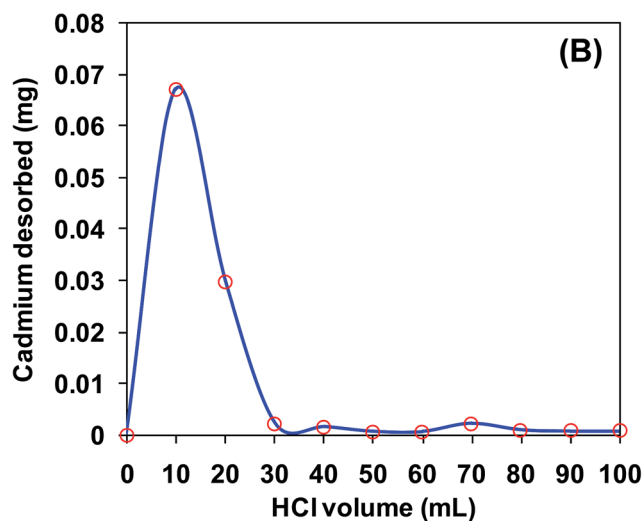
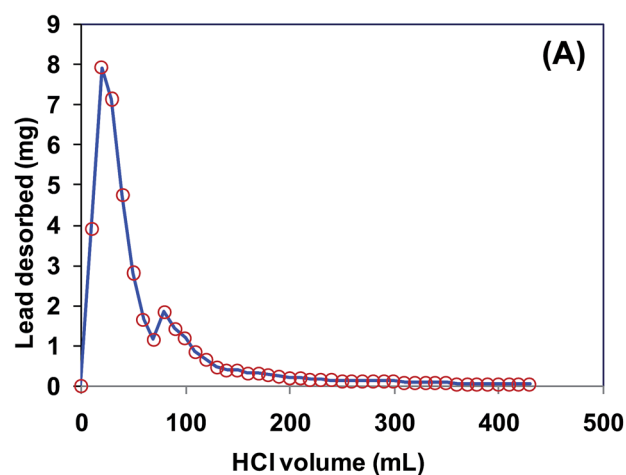


Fig. 15 KPP desorption curves for (a) Pb^{2+} and (b) Cd^{2+} using 0.1 N HCl.



concentrations analyzed. Cd^{2+} and Pb^{2+} concentrations were reduced by adsorption (Table 5), showing both KPP and MKPP could be successfully removed Cd^{2+} and Pb^{2+} from groundwater.

3.9. Column studies

3.9.1. Fixed-bed Pb^{2+} sorption and desorption studies. Pb^{2+} removal using a fixed-bed of KPP was studied. The column set-up is shown in Fig. SM1.† To an acrylic column (length = 40 cm; diameter = 20 mm) 5 g KPP (30–50 B.S.S. mesh) was added, supported by glass wool. The KPP bed height was 6 cm. A Pb^{2+} solution (conc. = 10 mg L^{-1}) passed continuously through under gravity@ 5 mL min^{-1} until the exhaustion point was reached. The breakthrough curve expressed in terms of C/C_0 versus the sorption volume of aqueous Pb^{2+} on KPP is shown in Fig. 14.^{87,88} The total time involved for establishment of primary adsorption zone (t_x) (eqn (10)), the time for the primary adsorption zone (PAZ) to move down its length (t_b) (eqn (11)), the length of the primary adsorption zone (δ) (eqn (12)), the fractional capacity (f) (eqn (13)), the bed depth (D) (eqn (14)), the time required for initial PAZ formation (t_b) (eqn (12)–(14)), the mass rate of flow to

the adsorber (F_m) (eqn (11)), the percent saturation of column at breakthrough (eqn (15)) were obtained. The bed volume (eqn (16)), the empty-bed-contact-time (EBCT) (eqn (17)) and the biomass usage rate (eqn (18)) were also calculated. Table 6 lists the values of these fixed bed column parameters.⁸⁷

$$t_x = \frac{\bar{V}_x}{F_m} \quad (10)$$

$$t_b = \frac{\bar{V}_x - \bar{V}_b}{F_m} \quad (11)$$

$$\frac{\delta}{D} = \frac{t_b}{t_x - t_b} \quad (12)$$

$$f = 1 - \frac{t_b}{t_x} \quad (13)$$

$$\delta = D \left(1 - \frac{t_b}{t_x} \right) \quad (14)$$

Table 7 Comparison of Langmuir adsorption capacities of KPP and MKPP versus other biosorbents for Pb^{2+} and Cd^{2+} remediation from water

Biosorbent	Initial pH	Temp. (°C)	Conc. range (mg L^{-1})	Langmuir adsorption capacity (mg g^{-1})	Reference
[A] Pb^{2+}					
KPP	4.5	25	5–100	16.37	This study
MKPP	4.5	25	5–100	14.14	This study
Banana peels	5.0	25	30–80	2.2	90
Ground nut husk modified with Gaur gum	5.0	25	20–100	9.8	91
<i>Eupatorium adenophorum</i> Spreng	5.0	26	10–50	3.5	92
Poplar tree branch	4.0	25	1–10	1.7	93
Pomegranate peel	5.6	26	10–50	13.9	94
<i>Saccharomyces cerevisiae</i>	—	—	—	41.9	95
<i>S. polyrhiza</i> biomass	4.0	20	100–160	124.0	96
Polyamic acid grafted bakers's yeast biomass	—	—	—	204.5	97
Nitrilotriacetic acid anhydride modified ligno-cellulosic material	4.0	25	20–600	304	20
		30		309	
		40		326	
Waste biomass from biotrickling filters	5.0	25	10–200	160	82
[B] Cd^{2+}					
KPP	5.0	25	2–100	11.1	This study
MKPP	5.0	25	2–100	4.8	This study
<i>Moringa oleifera</i> Lamarck seed	6.5	—	10–50	1.4	98
Rice husk	6.6–6.8	28–30	—	8.6	99
Coconut copra	6.0	26	10.5–201	4.9	7
		38		4.7	
		50		2.7	
		60		2.0	
<i>Caulerpa lentillifera</i>	5	21	—	4.9	100
	4			4.7	
	3			2.0	
Eucalyptus bark	5.0	30	25–300	11.60	101
Banana peels	3.0	25	30–80	5.71	90
<i>Saccharomyces cerevisiae</i>	—	—	—	41.9	95
<i>S. polyrhiza</i> biomass	4.0	20	100–160	124.0	96
Polyamic acid grafted bakers's yeast biomass	—	—	—	204.5	97
Nitrilotriacetic acid anhydride modified ligno-cellulosic material	3.8	25	20–500	143	20
		30		151	
		40		163	



$$\text{Percent saturation} = \frac{D + \delta(f - 1)}{D} \times 100 \quad (15)$$

$$\text{Bed volume} = \frac{\text{weight of biomass (kg)}}{\text{biomass bulk density (kg m}^{-3}\text{)}} \quad (16)$$

$$\text{EBCT} = \frac{\text{bed volume}}{\text{flow rate}} \quad (17)$$

$$\begin{aligned} \text{Biomass usage rate (kg L}^{-1}\text{)} \\ = \frac{\text{weight of biomass in column (g)}}{\text{volume of breakthrough (L)}} \end{aligned} \quad (18)$$

here, V_b and V_x are total effluent mass quantity per unit adsorbent area at the breakpoint, and the total effluent mass quantity per unit adsorbent area when adsorbent is approaching saturation, respectively. C_b and C_x are the effluent concentrations at V_b and V_x , respectively. The performance in a packed column can be characterized by the shape of the breakthrough curve.^{87,88} An 'S' shaped breakthrough curve was obtained for Pb^{2+} sorption on KPP (Fig. 14).

The column capacity was slightly higher (18.8 mg g^{-1}) than batch capacity (16.4 mg g^{-1}) for Pb^{2+} removal. This is because a large Pb^{2+} concentration gradient is continuously present at KPP interface.

pH changes occurred during column experiments. The equilibrium pH initially increased to 5.5, possibly because of adsorption of the H_3O^+ from the solution. Furthermore, equilibrium pH decreased to pH 3.99 at the breakpoint as the column attained saturation, where no more H_3O^+ adsorption occurred (Fig. 14). At the exhaustion point, the equilibrium pH was similar to the initial pH (4.5) (Fig. 14). This confirmed that no further Pb^{2+} uptake occurred beyond the exhaustion point. Similar observations were reported earlier.⁸⁹

Lead desorption from KPP was performed using 10 mL increments of 0.1 N HCl at the same flow rate and bed height (Fig. 15). About 85% of total Pb^{2+} desorption was achieved using first ten aliquots (total 100 mL) of HCl. The remaining Pb^{2+} was desorbed in successive increments.

Cadmium desorption was performed in batch mode using 10 mL increments of 0.1 N HCl. Initially, 50 mL of $100 \text{ mg L}^{-1} \text{ Cd}^{2+}$ solution (pH 5.0) was agitated with 4 g L^{-1} KPP for 24 h (Fig. 15). The suspension was then filtered and KPP biosorbent was desorbed using 10 mL 0.1 N HCl. Approximately 63% of the total cadmium desorption was achieved in first 10 aliquot (total 10 mL) of HCl. The KPP and MKPP biosorbents were highly stable under acidic aqueous medium. Both KPP and MKPP samples were suspended in acidic water (0.1, 0.2, 0.5, 1 and 2 N HCl). No significant leaching of iron was observed during the period of twelve hours.

4. Conclusions

Bauhinia purpurea (Kaniar) pods were dried, powdered and utilized for cadmium and lead removal. *Bauhinia purpurea* (Kaniar) pod powders (KPP) were converted into magnetic *Bauhinia purpurea* (Kaniar) powders (MKPP) by magnetite

precipitation onto KPP. KPP and MKPP were characterized and used for Cd^{2+} and Pb^{2+} sorptive removal. Optimum removal occurred at pH 5.0 and 4.5 for Cd^{2+} and Pb^{2+} , respectively. Cd^{2+} and Pb^{2+} sorption mechanisms were established. Sorption equilibrium and dynamic studies were conducted. Among two parameter models, the Langmuir equation best described Cd^{2+} and Pb^{2+} adsorption, with capacities of 11.1 and 4.8 mg g^{-1} for Cd^{2+} and 24.0 and 20.0 mg g^{-1} for Pb^{2+} obtained on KPP and MKPP, respectively. Among three parameter models, Redlich–Peterson and Radke–Prausnitz equations were best fitted to Cd^{2+} sorption and Sips model best fitted to Pb^{2+} sorption data. Langmuir adsorption capacities of KPP and MKPP for Pb^{2+} and Cd^{2+} were comparable to other biosorbents (Table 7). Sorption dynamics data was obtained and best fitted to pseudo-second order kinetics for Cd^{2+} and Pb^{2+} . Chemisorption was the rate controlling mechanism. Adsorption thermodynamics parameters were calculated (Table 4). Cd^{2+} and Pb^{2+} adsorption was spontaneous. Cd^{2+} adsorption was exothermic whereas Pb^{2+} sorption was endothermic as evidenced by the ΔH° values. Cd^{2+} and Pb^{2+} were successfully removed in a multi-ion aqueous environment of Cd^{2+} , Pb^{2+} , and Cu^{2+} . Removal of Cd^{2+} and Pb^{2+} from actual groundwater using KPP and MKPP was also demonstrated.

Fixed-bed Pb^{2+} removal using KPP exhibited a column capacity of 18.8 mg g^{-1} . Regeneration of spent KPP in the column using 0.1 N HCl gave an 85% recovery of total Pb^{2+} using the first ten aliquots of HCl and the remaining Pb^{2+} was recovered in further increments.

Acknowledgements

One of the authors, RS, thankfully acknowledges the financial support for this work provided by CSIR. Authors are also thankful to University Grant Commission (UGC), New Delhi for providing the financial assistance under 21st Century Indo-US Research Initiative 2014 to Jawaharlal Nehru University, New Delhi and Mississippi State University, USA in the project "Clean Energy and Water Initiatives" [UGC No. F.194-1/2014(IC)]. One of the authors (DM) is also thankful to Jawaharlal Nehru University for providing financial assistance under Second phase of University with Potential of Excellence (UPOE II) grant (ID 189). Authors also acknowledge the funding support from DST PURSE, Government of India. The study is also supported by Indo-Sri Lankan joint research project grant (No. INT/SL/12/P-008) provided by Department of Science and Technology (DST), Government of India.

References

- V. K. Singh, D. S. Bikundia, A. Sarswat and D. Mohan, *Environ. Monit. Assess.*, 2012, **184**, 4473–4488.
- J. Fawell and M. J. Nieuwenhuijsen, *Br. Med. Bull.*, 2003, **68**, 199–208.
- S. Chouhan and S. J. S. Flora, *Indian J. Exp. Biol.*, 2010, **48**, 666–678.
- M. Kumari, C. U. Pittman Jr and D. Mohan, *J. Colloid Interface Sci.*, 2015, **442**, 120–132.



- 5 D. Mohan, H. Kumar, A. Sarswat, M. Alexandre-Franco and C. U. Pittman Jr, *Chem. Eng. J.*, 2014, **236**, 513–528.
- 6 M. Tsezos, *Hydrometallurgy*, 2001, **59**, 241–243.
- 7 Y.-S. Ho and A. E. Ofomaja, *Biochem. Eng. J.*, 2006, **30**, 117–123.
- 8 D. Mohan, C. U. Pittman Jr, M. Bricka, F. Smith, B. Yancey, J. Mohammad, P. H. Steele, M. F. Alexandre-Franco, V. Gómez-Serrano and H. Gong, *J. Colloid Interface Sci.*, 2007, **310**, 57–73.
- 9 *Environmental Inorganic Chemistry: Properties, Processes, and Estimation Methods*, ed. W. J. Lyman, W. F. Reehl and D. H. Rosenblatt, Pergamon press, New York, 1988.
- 10 P. Grover, P. V. Rekhadevi, K. Danadevi, S. B. Vuyyuri, M. Mahboob and M. F. Rahman, *Int. J. Hyg. Environ. Health*, 2010, **213**, 99–106.
- 11 E. M. Mager, K. V. Brix, K. R. M. Gerdes, A. C. Ryan and M. Grosell, *Ecotoxicol. Environ. Saf.*, 2011, **74**, 238–243.
- 12 L. Järup, *Br. Med. Bull.*, 2003, **68**, 167–182.
- 13 WHO, *WHO Guidelines for Drinking-Water Quality*, WHO Press, Geneva, 4th edn, 2011.
- 14 BIS, Bureau of Indian Standard, *Indian standard specification for drinking water*, BIS, Delhi, IS 10500, 1991, pp. 2–4.
- 15 BIS, *Drinking Water Specification*, Second Revision IS: 10500: 2012, Bureau of Indian Standards, New Delhi, India, 2012.
- 16 K. S. Low, C. K. Lee and S. C. Liew, *Process Biochem.*, 2000, **36**, 59–64.
- 17 K. Y. Foo and B. H. Hameed, *J. Hazard. Mater.*, 2010, **175**, 1–11.
- 18 S. K. R. Yadanaparthi, D. Graybill and R. v. Wandruszka, *J. Hazard. Mater.*, 2009, **171**, 1–15.
- 19 O. Yavuz, R. Guzel, F. Aydin, I. Tegin and R. Ziyadanogullari, *Pol. J. Environ. Stud.*, 2007, **16**, 467.
- 20 Y. Huang, C. Yang, Z. Sun, G. Zeng and H. He, *RSC Adv.*, 2015, **5**, 11475–11484.
- 21 J. Wang and C. Chen, *Biotechnol. Adv.*, 2006, **24**, 427–451.
- 22 J. Wang and C. Chen, *Biotechnol. Adv.*, 2009, **27**, 195–226.
- 23 A. Jusoh, L. S. Shiung, N. a. Ali and M. J. M. M. Noor, *Desalination*, 2007, **206**, 9–16.
- 24 T. Robinson, G. McMullan, R. Marchant and P. Nigam, *Bioresour. Technol.*, 2001, **77**, 247–255.
- 25 E. Fourest, C. Canal and J. C. Roux, *FEMS Microbiol. Rev.*, 1992, **14**, 325–332.
- 26 K. Mohanty, M. Jha, B. C. Meikap and M. N. Biswas, *Chem. Eng. J.*, 2006, **117**, 71–77.
- 27 A. Moubarik and N. Grimi, *Food Res. Int.*, 2015, **73**, 169–175.
- 28 C. Pennesi, C. Totti, T. Romagnoli, B. Bianco and I. D. Michelis, *Water Environ. Res.*, 2012, **84**, 9–16.
- 29 S. Balaji, T. Kalaivani, C. Rajasekaran, M. Shalini, R. Siva, R. K. Singh and M. A. Akthar, *Clean: Soil, Air, Water*, 2014, **42**, 1790–1797.
- 30 D. Sharmila and P. Muthusamy, *J. Chem. Pharm. Res.*, 2013, **5**, 10–13.
- 31 A. Jakóbk-Kolon, A. K. Milewski, K. Mitko and A. Lis, *Sep. Sci. Technol.*, 2014, **49**, 1679–1688.
- 32 Z. R. Holan and B. Volesky, *Appl. Biochem. Biotechnol.*, 1995, **53**, 133–146.
- 33 C. K. Jain, D. S. Malik and A. K. Yadav, *Environ. Processes*, 2016, **3**, 495–523.
- 34 P. Krishen, *Trees of Delhi: a field guide*, Penguin Books, India, 2006.
- 35 T. K. Lim, *Bauhinia purpurea*, in *Edible Medicinal And Non-Medicinal Plants*, Springer, Netherlands, 2014, pp. 743–753.
- 36 H. V. Annegowda, M. N. Mordi, S. Ramanathan, M. R. Hamdan and S. M. Mansor, *Food Analytical Methods*, 2012, **5**, 226–233.
- 37 E. F. Fang, C. S. F. Bah, J. H. Wong, W. L. Pan, Y. S. Chan, X. J. Ye and T. B. Ng, *Arch. Toxicol.*, 2012, **86**, 293–304.
- 38 B. S. Negi, B. P. Dave and Y. K. Agarwal, *Indian J. Microbiol.*, 2012, **52**, 360–365.
- 39 N. Neelapu and S. Muvvala, *Int. J. Res. Phytochem. Pharmacol.*, 2012, **1**, 97–102.
- 40 A. Kanwal, S. A. Mirza and M. Farhan, *Pak. J. Bot.*, 2015, **47**, 275–280.
- 41 K. Polipalli and K. Pulipati, *Int. J. Sci. Eng. Res.*, 2013, **4**, 1244–1252.
- 42 E. P. Barrett, L. G. Joyner and P. P. Halenda, *J. Am. Chem. Soc.*, 1951, **73**, 373–380.
- 43 M. M. Dubinin, in *Progress in Surface and Membrane Science*, ed. D. A. Cadenhead, J. F. Danielli and M. D. Rosenberg, Academic Press, New York and London, 1975, pp. 1–70.
- 44 M. M. Dubinin and G. M. Plavnik, *Carbon*, 1968, **6**, 183–192.
- 45 ASTM-D1762-84, *ASTM International, Standard test method for chemical analysis of wood charcoal*, ASTM International, Pennsylvania, 2007.
- 46 H. M. F. Freundlich, *J. Phys. Chem.*, 1906, **57**, 385–471.
- 47 I. Langmuir, *J. Am. Chem. Soc.*, 1916, **38**, 2221–2295.
- 48 M. I. Temkin and V. Pyzhev, *Acta physicochimica U.R.S.S.*, 1940, **12**, 217–222.
- 49 R. Sips, *J. Chem. Phys.*, 1948, **16**, 490–495.
- 50 O. Redlich and D. L. Peterson, *J. Phys. Chem.*, 1959, **63**, 1024.
- 51 C. J. Radke and J. M. Prausnitz, *Ind. Eng. Chem. Fundam.*, 1972, **11**, 445–451.
- 52 J. Toth, *Acta Chim. Acad. Sci. Hung.*, 1971, **69**, 311–317.
- 53 R. Koble and T. Corrigan, *Ind. Eng. Chem. Fundam.*, 1952, **44**, 383–387.
- 54 S. Lagergren, *Handlingar*, 1898, **24**, 1–7.
- 55 Y. S. Ho and G. McKay, *Process Biochem.*, 1999, **34**, 451.
- 56 D. Mohan and S. Chander, *J. Colloid Interface Sci.*, 2006, **299**, 76–87.
- 57 N. F. Cardoso, E. C. Lima, I. S. Pinto, C. V. Amavisca, B. Royer, R. B. Pinto, W. S. Alencar and S. F. P. Pereira, *J. Environ. Manage.*, 2011, **92**, 1237–1247.
- 58 S. Nanda, P. Mohanty, K. K. Pant, S. Naik, J. A. Kozinski and A. K. Dalai, *BioEnergy Res.*, 2013, **6**, 663–677.
- 59 A. C. Correa, E. D. M. Teixeira, L. A. Pessan and L. H. C. Mattoso, *Cellul. Chem. Technol.*, 2010, **17**, 1183–1192.
- 60 S. V. Vassilev, D. Baxter, L. K. Andersen, C. G. Vassileva and T. J. Morgan, *Fuel*, 2012, **94**, 1–33.
- 61 K. Umamaheswaran and V. S. Batra, *Fuel*, 2008, **87**, 628–638.
- 62 T. Madrakian, A. Afkhami, M. Ahmadi and H. Bagheri, *J. Hazard. Mater.*, 2011, **196**, 109–114.



- 63 Q. Peng, Y. Liu, G. Zeng, W. Xu, C. Yang and J. Zhang, *J. Hazard. Mater.*, 2010, **177**, 676–682.
- 64 A. B. Albadarin, C. Mangwandi, G. M. Walker, S. J. Allen, M. N. M. Ahmada and M. Khraisheh, *J. Environ. Manage.*, 2013, **114**, 190–201.
- 65 J. R. Koduru, Y.-Y. Chang, J.-K. Yang and I.-S. Kim, *Sci. World J.*, 2013, **2013**, 1–14.
- 66 M. Namdeo and S. K. Bajpai, *Electron. J. Environ., Agric. Food Chem.*, 2009, **8**, 3082–3094.
- 67 K. Chitra and G. Annadurai, *Biocybern. Biomed. Eng.*, 2014, **34**, 230–237.
- 68 V. K. Singh and K. R. C. Reddy, *Int. J. Res. Phytochem. Pharmacol.*, 2015, **3**, 386–390.
- 69 S. S. Banerjee and D.-H. Chen, *J. Hazard. Mater.*, 2007, **147**, 792–799.
- 70 S. Yorgun and D. Yildiz, *J. Anal. Appl. Pyrolysis*, 2015, **114**, 68–78.
- 71 M. Fereidouni, A. Daneshi and H. Younes, *J. Hazard. Mater.*, 2009, **168**, 1437–1448.
- 72 A. M. Petrosyan, *Vib. Spectrosc.*, 2007, **43**, 284–289.
- 73 H. Schulz and M. Baranska, *Vib. Spectrosc.*, 2007, **43**, 13–25.
- 74 S. H. Kim, C. M. Lee and K. Kafle, *Korean J. Chem. Eng.*, 2013, **30**, 2127–2141.
- 75 A. Ahmad, M. Rafatullah, O. Sulaiman, M. H. Ibrahim, Y. Y. Chii and B. M. Siddique, *Desalination*, 2009, **247**, 636–646.
- 76 D. Asandei, L. Bulgariu and E. Bobu, *Cellul. Chem. Technol.*, 2009, **43**, 211–216.
- 77 K. Chojnacka, A. Chojnacki and H. Gorecka, *Chemosphere*, 2005, **59**, 75–84.
- 78 Y. Ding, D. Jing, H. Gong, L. Zhou and X. Yang, *Bioresour. Technol.*, 2012, **114**, 20–25.
- 79 T. Kumar and K. S. Chandrashekar, *Res. J. Med. Plants*, 2011, **5**, 420–431.
- 80 Z. Wang, G. Liu, H. Zheng, F. Li, H. H. Ngo, W. Guo, C. Liu, L. Chen and B. Xing, *Bioresour. Technol.*, 2015, **177**, 308–317.
- 81 W.-J. Liu, F.-X. Zeng, H. Jiang and H.-Q. Yu, *Cellul. Chem. Technol.*, 2011, **50**, 5920–5926.
- 82 Y. Cheng, C. Yang, H. He, G. Zeng, K. Zhao and Z. Yan, *J. Environ. Eng.*, 2016, **142**, C4015001, DOI: 10.1061/(asce)ee.1943-7870.0000956.
- 83 C. Yang, J. Wang, M. Lei, G. Xie, G. Zeng and S. Luo, *J. Environ. Sci.*, 2010, **22**, 675–680.
- 84 T. A. Davis, B. Volesky and A. Mucci, *Water Res.*, 2003, **37**, 4311–4330.
- 85 K. R. Hall, L. C. Eagleton, R. Acrivos and T. Vermeulen, *Ind. Eng. Chem. Fundam.*, 1966, **5**, 212–223.
- 86 D. Mohan, A. Sarswat, V. K. Singh, M. Alexandre-Franco and C. U. Pittman Jr, *Chem. Eng. J.*, 2011, **172**, 1111–1125.
- 87 A. Sarswat and D. Mohan, *RSC Adv.*, 2016, **6**, 85390–85410.
- 88 W. J. Weber Jr, *Physicochemical Processes for Water Quality Control*, Wiley, 1972.
- 89 A. H. Hawari and C. N. Mulligan, *Process Biochem.*, 2006, **41**, 187–198.
- 90 J. Anwar, U. Shafique, Waheed-uz-Zaman, M. Salman, A. Dar and S. Anwar, *Bioresour. Technol.*, 2010, **101**, 1752–1755.
- 91 R. Ahmad and S. Haseeb, *Groundwater for Sustainable Development*, 2015, vol. 1, pp. 41–49.
- 92 S. Guo, L. Z. Wei Li, J. Peng, H. Xia and S. Zhang, *Process Saf. Environ. Prot.*, 2009, **87**, 343–351.
- 93 M. S. Al-Masri, Y. A. B. Al-Akel and T. Al-Naama, *Appl. Biochem. Biotechnol.*, 2010, **160**, 976–987.
- 94 E. S. Z. El-Ashtoukhy, N. K. Amin and O. Abdelwaha, *Desalination*, 2008, **223**, 162–173.
- 95 M. Al-Saraj, M. S. Abdel-Latif, I. El-Nahal and R. Barak, *J. Non-Cryst. Solids*, 1999, **248**, 37–40.
- 96 M. D. Meitei and P. N. V. Majeti, *Ecol. Eng.*, 2014, **71**, 308–317.
- 97 J. Yu, M. Tong, X. Sun and B. Li, *React. Funct. Polym.*, 2007, **67**, 564–572.
- 98 M. Rajeswari, P. Agrawal, S. Pavithra, Priya, G. R. Sandhya and G. M. Pavithra, *Biotechnol. Bioprocess Eng.*, 2013, **18**, 321–325.
- 99 U. Kumar and M. Bandyopadhyay, *Bioresour. Technol.*, 2006, **97**, 104–109.
- 100 P. Pavasant, R. Apiratikul, V. Sungkhum, P. Suthiparinyanont, S. Wattanachira and T. F. Marhaba, *Bioresour. Technol.*, 2006, **97**, 2321–2329.
- 101 I. Ghodbane, L. Nouri, O. Hamdaoui and M. Chiha, *J. Hazard. Mater.*, 2008, **152**, 148–158.

